

# METALLICITIES OF $0.3 < z < 1.0$ GALAXIES IN THE GOODS-NORTH FIELD

HENRY A. KOBULNICKY

Department of Physics and Astronomy, University of Wyoming, Laramie, WY 82071; chipk@uwyo.edu

AND

LISA J. KEWLEY

Smithsonian Astrophysical Observatory, Mail Stop 20, 60 Garden Street, Cambridge, MA 02138; lkewley@cfa.harvard.edu

Received 2004 June 2; accepted 2004 August 5

## ABSTRACT

We measure nebular oxygen abundances for 204 emission-line galaxies with redshifts  $0.3 < z < 1.0$  in the Great Observatories Origins Deep Survey–North (GOODS-N) field using spectra from the Team Keck Redshift Survey. We also provide an updated analytic prescription for estimating oxygen abundances using the traditional strong emission line ratio,  $R_{23}$ , based on the photoionization models of Kewley & Dopita. We include an analytic formula for very crude metallicity estimates using the  $[\text{N II}]_{\lambda 6584}/\text{H}\alpha$  ratio. Oxygen abundances for GOODS-N galaxies span the range  $8.2 \leq 12 + \log(\text{O}/\text{H}) < 9.1$ , corresponding to metallicities between 0.3 and 2.5 times the solar value. This sample of galaxies exhibits a correlation between rest-frame blue luminosity and gas-phase metallicity (i.e., an  $L$ - $Z$  relation), consistent with  $L$ - $Z$  correlations of previously studied intermediate-redshift samples. The zero point of the  $L$ - $Z$  relation evolves with redshift, in the sense that galaxies of a given luminosity become more metal-poor at higher redshift. Galaxies in luminosity bins  $-18.5 < M_B < -21.5$  exhibit a decrease in average oxygen abundance by  $0.14 \pm 0.05$  dex from  $z = 0$  to 1. This rate of metal enrichment means that  $28\% \pm 0.07\%$  of metals in local galaxies have been synthesized since  $z = 1$ , in reasonable agreement with the predictions based on published star formation rate densities, which show that  $\sim 38\%$  of stars in the universe have formed during the same interval. The slope of the  $L$ - $Z$  relation may evolve, in the sense that the least luminous galaxies at each redshift interval become increasingly metal-poor compared to more luminous galaxies. We interpret this change in slope as evidence for more rapid chemical evolution among the least luminous galaxies ( $M_B > -20$ ), consistent with scenarios whereby the formation epoch for less massive galaxies is more recent than for massive galaxies.

*Subject headings:* galaxies: abundances — galaxies: evolution — galaxies: fundamental parameters — galaxies: starburst — H II regions — ISM: abundances

*On-line material:* color figures, machine-readable table

## 1. METALLICITY IN GALAXY EVOLUTION AND MODELING

The chemical composition of galaxies is fundamentally important for tracing galaxy evolution and for modeling galaxy properties. Galaxy evolution prescriptions dating from Tinsley (1974, 1980) to present computational codes (e.g., STARBURST99: Leitherer et al. 1999; Bruzual & Charlot 2003; Pégase: Fioc & Rocca-Volmerange 1999; GRASIL: Silva et al. 1998) incorporate metallicity as a primary ingredient in tracking a galaxy’s growth. Metallicity determines a galaxy’s UV and optical colors at a given age, the strength of stellar and interstellar metallic absorption lines, the shape of its interstellar extinction curve (e.g., Prévot et al. 1984), its dust-to-gas ratio (Dwek 1998; Issa et al. 1990), its nucleosynthetic yields (e.g., Woosley & Weaver 1995), and perhaps even its rate of star formation (Nishi & Tashiro 2000). Overall metal abundance and elemental abundance ratios trace the star formation history and nucleosynthetic history of a galaxy (reviewed by Wheeler et al. 1989). These abundances and ratios also reflect the importance of gas inflow and outflow in a galaxy’s evolution (galactic winds, Matthews & Baker 1971; metal-rich galactic winds, Vader 1987). Observational studies have now begun to provide detailed optical and infrared measurements of thousands of galaxies at redshifts from 0.1 to 6 (e.g., Rowan-Robinson 2001; Hippelein et al. 2003; Sullivan et al. 2004; van

Dokkum et al. 2004; Steidel et al. 2004 and references therein), spanning the vast majority of cosmic time. Successful modeling of the evolutionary paths of these galaxies will require, among other parameters, secure measurements of their chemical compositions.

Direct measurements of metallicities<sup>1</sup> in distant galaxies are now becoming routine, spurred on by the larger telescopes and more capable spectrographs used in deep galaxy surveys. Kobulnicky & Zaritsky (1999) first applied classical nebular diagnostic techniques developed for H II regions in local galaxies to the global spectra of 14 compact star-forming galaxies at  $0.1 < z < 0.5$ . Their sample spanned the range of galaxy luminosities  $-17 > M_B > -22$  and oxygen abundances  $8.25 < 12 + \log(\text{O}/\text{H}) < 9.02$ .<sup>2</sup> Carollo & Lilly (2001) presented oxygen abundances for 15 luminous galaxies from the Canada-France Redshift Survey (CFRS; Lilly et al. 1995) over the range  $0.60 < z < 0.98$  and  $-20.1 > M_B > -22.6$ .

<sup>1</sup> In this work we focus primarily on *nebular oxygen abundance* as a tracer of overall gas-phase *metallicity*, and we use the terms interchangeably. Other metallicity indicators being explored in distant galaxies include interstellar absorption lines (Savaglio et al. 2004) and stellar photospheric absorption lines (Mehlert et al. 2002).

<sup>2</sup> We take the solar oxygen abundance to be  $12 + \log(\text{O}/\text{H})_{\odot} \simeq 8.7$  based on the solar oxygen abundance determination of Allende Prieto et al. (2001).

Both of these early works concluded that intermediate-redshift galaxies were consistent with the same correlation between luminosity and metallicity (i.e., the  $L$ - $Z$  relation) observed in local samples (e.g., Faber 1973; Lequeux et al. 1979; Skillman et al. 1989; Zaritsky et al. 1994, hereafter ZKH94). Meanwhile, Kobulnicky & Koo (2000), Pettini et al. (2001), and Shapley et al. (2004) used near-infrared spectroscopy of  $2.1 < z < 3.5$  Lyman break galaxies to measure gas-phase oxygen abundances. These authors concluded that the high-redshift objects were 2–4 mag more luminous than  $z = 0$  galaxies with comparable  $8.3 < 12 + \log(\text{O}/\text{H}) < 9$  metallicities and thus were inconsistent with the local  $L$ - $Z$  relation. Evidence for evolution of the  $L$ - $Z$  relation with epoch, particularly among sub- $L^*$  galaxies with  $M_B$  fainter than  $-20$ , grew with metallicity measurements of 64  $0.26 < z < 0.82$  field galaxies in the Groth Strip Survey (DGSS; Kobulnicky et al. 2003, hereafter Ke03) and 66 additional CFRS galaxies at  $0.47 < z < 0.92$  (Lilly et al. 2003, hereafter LCS03; Carollo & Lilly 2001, hereafter CL01). Recently, Maier et al. (2004) measured metallicities for five sub- $L^*$  galaxies at  $z \sim 0.4$  and 10 sub- $L^*$  galaxies at  $z \sim 0.64$  from the CADIS emission-line survey. These additional sub- $L^*$  galaxies provide further support for the evolution of the  $L$ - $Z$  relation with epoch.

In this paper we present gas-phase oxygen abundance measurements for 204 emission-line galaxies from  $0.3 < z < 0.93$  in the Great Observatories Origins Deep Survey–North (GOODS-North; Giavalisco et al. 2004) field using the publicly available spectra obtained as part of the Team Keck Treasury Redshift Survey (TKRS; Wirth et al. 2004). The new data double the number of metallicities previously available for this redshift range and constitute the highest quality spectra yet available for chemical analysis. In addition to providing new constraints on the chemical enrichment of galaxies over the last 8 Gyr, it is our hope that these measurements will prove useful for the community in modeling the evolution of galaxies in this well-studied cosmological field. We combine these new TKRS data with existing emission-line measurements from the literature (CFRS, LCS03; DGSS, Kobulnicky et al. 2003) to assess the chemoluminous evolution of star-forming galaxies out to  $z = 1$ . Where applicable, we adopt a cosmology with  $H_0 = 70 \text{ km s}^{-1} \text{ Mpc}^{-1}$ ,  $\Omega_m = 0.3$ , and  $\Omega_\Lambda = 0.7$ .

## 2. DATA ANALYSIS

### 2.1. Target Selection

The TKRS consists of Keck telescope spectroscopy with the DEIMOS (Faber et al. 2003) spectrograph over the nominal wavelength range 4600–9800 Å. Targets include both stars and galaxies, selected in an unbiased manner from all objects with  $R \leq 24.4$  in ground-based optical images (Wirth et al. 2004). Slit masks with  $1''$  wide slits tilted to align with a galaxy’s major axis provided up to 100 spectra per 1200 s exposure. Spectra have typical resolutions of  $\sim 3.5 \text{ Å}$  and total integration times of 3600 s.

We searched the publicly available TKRS spectroscopic database for galaxies with nebular emission lines suitable for chemical analysis. Only galaxies for which it was possible to measure all of the requisite [O II]  $\lambda 3727$ , H $\beta$ , and [O III]  $\lambda 5007$  lines were retained. These criteria necessarily exclude objects at redshifts of  $z \lesssim 0.3$ , since the requisite [O II]  $\lambda 3727$  line falls below the blue limit of the spectroscopic setup. Likewise, objects with redshifts  $z \gtrsim 1.0$  are excluded because the [O III]  $\lambda 5007$  line falls beyond the red wavelength limit of the survey. In the 2004 February public release of the TKRS, there were

1536 objects with secure redshifts. Of these, 1044 fell within our redshift limits. Of the 1044 candidates, 497 were removed from consideration because no emission lines were present in the spectrum. Next, 94 galaxies were removed from the sample because one of the requisite strong emission lines fell off the end of the wavelength coverage (or in between the red and blue spectral regions) because of the object’s placement on the slit mask. Following Kobulnicky et al. (2003), we removed 94 objects in the redshift ranges  $0.410 < z < 0.426$ ,  $0.52 < z < 0.54$ , and  $0.56 < z < 0.58$ . For these intervals, atmospheric O<sub>2</sub> absorption troughs between 6865 and 6920 Å (the “B band”) and between 7585 and  $\sim 7680 \text{ Å}$  (the “A band”) prohibit accurate measurement of emission lines. Another 122 objects were removed from the sample because the H $\beta$  emission line was absent or too weak ( $S/N < 8:1$ ) for reliable chemical determinations (see Kobulnicky et al. 1999 for a discussion of errors and uncertainties). The spectra of objects rejected because of a weak H $\beta$  line are usually dominated by stellar continuum rather than nebular emission from star-forming regions. Most local early-type spirals and elliptical galaxies share these spectral characteristics. For these objects, H $\beta$  is seen in absorption against the stellar spectrum of the galaxy. Thus, early-type galaxies with older stellar populations are preferentially rejected in favor of late-type galaxies with higher star formation rates (SFRs). An additional 31 galaxies had to be rejected because some combination of strong night-sky emission bands, low continuum, or poor continuum subtraction caused the extracted one-dimensional spectrum to have continuum levels that were either negative or very close to zero. Because chemical analysis requires emission lines powered by normal stellar ionizing radiation fields (as opposed to nonthermal sources from active galactic nuclei), we rejected nine objects exhibiting canonical active galactic nucleus or LINER signatures: broad emission lines (two objects) or  $\text{EW}_{[\text{Ne III}]\lambda 3826}/\text{EW}_{[\text{O II}]\lambda 3727}$  ratios exceeding 0.4 (seven objects; e.g., Osterbrock 1989). The resulting usable sample contained 204 emission-line galaxies.

Twenty-seven of the 204 selected galaxies have measurable H $\beta$  but immeasurably weak ( $S/N < 3:1$ ) [O III] lines. In principle, such objects should be included in the sample to avoid introducing a metallicity bias, but it is not possible to compute reliable metallicities if the oxygen lines are not detected with signal-to-noise ratio ( $S/N$ ) of 8:1 or better. We have retained these objects in the sample and measure upper limits on the [O III] line strengths, which are used below to compute lower limits on oxygen abundances.

The 204 galaxies in our sample appear in Table 1, along with their TKRS identifications from Wirth et al. (2004) in column (2), their GOODS-N<sup>3</sup> designations in column (3), spectroscopic redshifts in column (4), TKRS  $R$ -band magnitude in column (5), and GOODS-N “ $i$ ” (F775W) photometry in column (6). From the observed magnitudes and known redshifts, we computed<sup>4</sup> rest-frame absolute blue magnitudes,  $M_B$ , and colors,  $U - B$ , which appear in columns (7) and (8), respectively, of Table 1.

In order to assess whether the 204 selected objects are representative of the GOODS-N TKRS galaxies with spectra in the  $0.3 < z < 1.0$  redshift range, Figure 1 shows histograms of their redshifts and photometric properties. The four panels

<sup>3</sup> The GOODS-N data descriptions, photometric catalogs, and publicly available data can be found at <http://www.stsci.edu/science/goods>.

<sup>4</sup> We are grateful to C. Willmer of the DEEP2 Redshift Survey Team (Davis et al. 2003) for computing the  $K$ -corrections. Details are presented in C. N. A. Willmer et al. (2004, in preparation).

TABLE 1  
GOODS-NORTH TKRS SELECTED GALAXIES

No.	ID	GOODS ID	z	R	i <sub>775W</sub>	M <sub>B</sub>	U − B	EW				SFR				O/H					
				(mag)	(mag)	(mag)	(mag)	[O II]	Hβ	[O III]	Hα/N II	(M <sub>⊙</sub> /yr)	CODE	log O <sub>32</sub>	R <sub>23</sub>	M91	KD	Avg.	N II	Final	
(1)	(2)	(3)	(4)	(5)	(6)	(7)	(8)	(9)	(10)	(11)	(12)	(13)	(14)	(15)	(16)	(17)	(18)	(19)	(20)	(21)	
1.....	3551	J123651.06+621732.0	0.31870	22.57	22.12	−18.24	0.630	40.9 ± 2.1	6.6 ± 0.5	16.5 ± 0.7	7.1	0.14	0	−0.39	6.67	8.5 ± 0.04	8.65	8.57	8.63	8.57 ± 0.15	
2.....	3792	J123656.21+621743.2	0.31911	24.21	24.00	−16.77	0.480	79.4 ± 6.5	39 ± 1.9	157.8 ± 1.8	...	0.22	0	0.29	5.78	8.66 ± 0.02	8.79	8.72	...	8.72 ± 0.15	
3.....	9483	J123652.47+621036.0	0.32036	22.18	21.89	−18.66	0.520	46.7 ± 4.9	13.3 ± 1.3	47.9 ± 1.5	10.43	0.43	0	0.01	6.18	8.59 ± 0.04	8.73	8.66	8.62	8.66 ± 0.15	
4.....	7972	J123658.06+621300.8	0.32040	22.73	22.45	−18.23	0.410	36.7 ± 3.4	17.1 ± 1.3	65.8 ± 1.7	17.35	0.37	0	0.25	5.36	8.69 ± 0.02	8.83	8.76	8.46	8.76 ± 0.15	
5.....	11168	J123704.28+621000.0	0.32129	23.35	23.07	−17.67	0.590	45.2 ± 7.4	10.4 ± 1.2	75.3 ± 1.5	>7.16	0.13	0	0.22	9.71	8.36 ± 0.07	8.51	8.43	<8.96	8.43 ± 0.16	
6.....	11004	J123703.91+621009.7	0.32144	22.45	22.21	−18.53	0.340	54.4 ± 3.1	14 ± 1.1	45.1 ± 1.4	>9	0.4	0	−0.08	6.21	8.58 ± 0.03	8.72	8.65	<8.65	8.65 ± 0.15	
7.....	12136	J123744.51+621411.1	0.32238	22.62	22.28	−18.24	0.530	37.7 ± 3.8	11.5 ± 1.0	36.3 ± 1.3	10.46	0.25	0	−0.01	5.48	8.66 ± 0.04	8.8	8.73	8.61	8.73 ± 0.15	
8.....	7105	J123715.86+621559.8	0.32930	23.58	23.38	−17.33	0.500	59.3 ± 9.9	33.9 ± 2.3	255.3 ± 3.2	>7.08	0.32	0	0.63	8.76	8.5 ± 0.03	8.52	8.51	<8.56	8.51 ± 0.15	
9.....	5152	J123725.33+621925.6	0.33519	24.22	23.66	−16.96	0.730	112.7 ± 13.0	16.3 ± 2.2	51.8 ± 2.6	...	0.11	0	−0.33	8.98	8.31 ± 0.10	8.57	8.44	...	8.44 ± 0.18	
10.....	9208	J123717.27+621356.8	0.33635	21.59	21.20	−19.36	0.650	49.8 ± 3.9	7.2 ± 0.9	23.0 ± 0.9	8.35	0.44	0	−0.33	7.91	8.41 ± 0.07	8.51	8.46	8.59	8.46 ± 0.16	
11.....	2476	J123617.96+621457.6	0.33690	21.48	21.06	−19.16	0.720	45.7 ± 5.2	7.5 ± 1.2	14.7 ± 1.2	6.37	0.38	0	−0.49	6.35	8.52 ± 0.09	8.68	8.60	8.64	8.6 ± 0.17	
12.....	1563	J123617.44+621551.6	0.37584	22.03	21.62	−19.18	0.700	51.9 ± 1.4	11.8 ± 0.5	14.3 ± 1.4	3.86	0.61	2	−0.55	4.79	8.66 ± 0.14	8.85	8.75	8.79	8.75 ± 0.2	
13.....	6493	J123704.02+621523.6	0.37593	22.53	22.08	−18.73	0.760	51.5 ± 3.8	7.5 ± 0.7	12.4 ± 2.5	4.76	0.25	2	−0.61	6.72	8.47 ± 0.17	8.63	8.55	8.69	8.55 ± 0.22	
14.....	2246	J123652.36+621910.1	0.38741	23.84	23.45	−17.73	0.360	89.2 ± 9.7	33.2 ± 2.8	141.8 ± 3.4	>21.04	0.46	1	0.2	6.56	8.11 ± 0.14	8.22	8.16	<8.36	8.16 ± 0.2	
15.....	2336	J123605.49+621331.4	0.38990	24.15	23.96	−17.27	0.360	26.2 ± 5.6	31.9 ± 3.7	61.9 ± 4.0	>14.98	0.29	1	0.37	2.59	7.43 ± 0.13	9.02	8.23	<8.59	8.23 ± 0.19	
16.....	4648	J123619.84+621229.9	0.39740	23.20	22.94	−18.30	0.480	82.5 ± 3.0	31 ± 1.4	135.9 ± 1.3	16.83	0.72	0	0.21	6.61	8.58 ± 0.01	8.7	8.64	8.46	8.64 ± 0.15	
17.....	4822	J123621.55+621227.2	0.39847	20.78	20.32	−20.52	0.840	13.2 ± 1.1	2.6 ± 0.3	3.9 ± 0.3	2.11	0.46	0	−0.52	3.71	8.78 ± 0.15	8.95	8.87	9.19	8.87 ± 0.21	
18.....	1475	J123605.97+621436.1	0.40836	22.16	21.80	−19.29	0.640	67.5 ± 4.2	10.8 ± 1.6	22.2 ± 1.1	4.85	0.62	0	−0.48	7.00	8.46 ± 0.08	8.6	8.53	8.74	8.52 ± 0.17	
19.....	11619	J123706.92+621000.1	0.43348	22.22	21.81	−19.43	0.690	28.4 ± 1.3	6.3 ± 0.5	6.9 ± 0.6	6.1	0.41	0	−0.61	4.25	8.72 ± 0.15	8.9	8.81	8.61	8.81 ± 0.21	
20.....	3203	J123613.96+621336.9	0.43407	23.69	23.36	−17.99	0.580	44.5 ± 3.3	12.3 ± 1.2	70.5 ± 2.0	...	0.21	0	0.19	8.04	8.47 ± 0.05	8.54	8.51	...	8.51 ± 0.15	
21.....	3741	J123616.66+621310.8	0.43720	24.08	23.53	−17.87	0.440	68.9 ± 6.4	30.1 ± 1.8	169.4 ± 2.2	...	0.47	0	0.39	7.42	8.54 ± 0.02	8.63	8.59	...	8.59 ± 0.15	
22.....	3709	J123713.29+621954.0	0.43785	20.81	20.26	−20.82	0.820	19.9 ± 0.6	9.1 ± 0.3	5.2 ± 0.8	2.42	2.14	2	−0.58	2.26	8.93 ± 0.12	9.07	9.00	9.0	9 ± 0.19	
23.....	9316	J123748.69+621724.3	0.43813	21.48	20.92	−20.17	0.820	13.2 ± 0.7	3.4 ± 0.2	1.7 ± 0.2	1.84	0.44	0	−0.88	2.75	8.87 ± 0.13	9.04	8.95	9.11	8.95 ± 0.19	
24.....	11986	J123643.03+620659.1	0.44359	21.83	21.34	−19.81	0.670	39.1 ± 2.4	9.4 ± 0.6	12.2 ± 0.7	...	0.87	0	−0.5	4.50	8.7 ± 0.03	8.88	8.79	...	8.79 ± 0.15	
25.....	12020	J123654.15+620821.8	0.44643	22.91	22.33	−18.77	0.810	31.9 ± 3.5	9.4 ± 1.4	14.8 ± 5.0	...	0.33	2	−0.33	4.09	8.75 ± 0.07	8.92	8.84	...	8.84 ± 0.16	
26.....	5630	J123733.46+621952.4	0.44676	22.63	22.11	−19.19	0.520	42.6 ± 2.2	8.2 ± 0.9	18.7 ± 2.6	...	0.43	2	−0.35	6.00	8.57 ± 0.05	8.72	8.65	...	8.65 ± 0.15	
27.....	8577	J123728.74+621553.1	0.45098	23.35	22.89	−18.58	0.480	54.7 ± 6.0	13.5 ± 2.0	48.9 ± 5.5	...	0.4	0	−0.04	6.68	8.55 ± 0.08	8.67	8.61	...	8.61 ± 0.17	
28.....	7111	J123642.92+621216.7	0.45375	21.21	20.76	−20.55	0.670	22.9 ± 1.8	7.3 ± 0.4	5.7 ± 1.0	...	1.34	0	−0.6	3.07	8.85 ± 0.14	9.01	8.93	...	8.93 ± 0.2	
29.....	2837	J123644.32+621737.2	0.45468	21.68	21.33	−20.08	0.450	52.1 ± 0.9	19 ± 0.4	64.2 ± 0.9	7.08	2.26	0	0.09	5.53	8.66 ± 0.01	8.8	8.73	8.86	8.73 ± 0.15	
30.....	5621	J123658.39+621549.0	0.45652	21.69	21.29	−20.16	0.420	82.1 ± 1.2	30.9 ± 0.7	97.7 ± 1.3	6.79	3.96	0	0.07	5.46	8.66 ± 0.01	8.81	8.74	8.87	8.74 ± 0.15	
31.....	5056	J123621.01+621204.3	0.45679	21.43	20.79	−20.08	0.810	26.9 ± 2.0	4.2 ± 0.5	8.0 ± 1.4	...	0.5	0	−0.52	5.62	8.59 ± 0.17	8.76	8.68	...	8.68 ± 0.22	
32.....	13261	J123802.24+621536.3	0.45686	21.60	21.28	−20.16	0.480	53.4 ± 4.4	13.2 ± 0.8	24.3 ± 1.5	...	1.69	0	−0.34	5.11	8.66 ± 0.03	8.82	8.74	...	8.74 ± 0.15	
33.....	5634	J123631.17+621236.7	0.45694	22.20	21.74	−19.69	0.560	81.8 ± 2.5	25.1 ± 0.9	58.9 ± 1.8	7.16	2.09	0	−0.14	5.19	8.67 ± 0.01	8.82	8.74	8.73	8.74 ± 0.15	
34.....	3272	J123605.01+621226.0	0.45724	23.89	23.4	−18.15	0.570	79.2 ± 4.9	29.6 ± 1.6	88.4 ± 2.8	43.44	0.6	0	0.04	5.30	8.67 ± 0.02	8.13	8.40	7.98	8.4 ± 0.15	
35.....	8525	J123725.16+621502.8	0.45766	22.11	21.60	−19.55	0.560	38.6 ± 2.9	9.9 ± 1.0	18.8 ± 2.7	...	0.72	0	−0.31	4.82	8.68 ± 0.04	8.85	8.77	...	8.77 ± 0.15	
36.....	2964	J123604.25+621244.1	0.45776	23.77	23.23	−18.19	0.550	60.8 ± 6.6	12.7 ± 1.4	21.1 ± 2.8	...	0.26	0	−0.45	5.57	8.6 ± 0.07	8.77	8.68	...	8.68 ± 0.16	
37.....	6480	J123633.74+621156.8	0.45859	22.42	21.95	−19.23	0.540	44.7 ± 3.1	14.1 ± 1.4	19.7 ± 1.6	...	0.77	0	−0.35	4.00	8.76 ± 0.03	8.93	8.84	...	8.84 ± 0.15	
38.....	6215	J123637.64+621241.3	0.45873	21.21	21.08	−20.27	0.580	39.5 ± 1.9	9.2 ± 0.8	30.8 ± 1.9	9.88	1.3	0	−0.1	6.27	8.58 ± 0.03	8.71	8.64	8.6	8.64 ± 0.15	
39.....	1217	J123621.26+621640.4	0.45874	22.01	21.61	−19.78	0.540	49.4 ± 1.2	16.8 ± 0.5	46.5 ± 0.6	8.48	1.52	0	−0.02	5.10	8.69 ± 0.01	8.84	8.76	8.71	8.76 ± 0.15	
40.....	2296	J123552.40+621204.1	0.45886	22.66	22.18	−19.16	0.490	72.3 ± 7.9	25 ± 3.1	51.6 ± 11.7	...	1.28	2	−0.14	4.58	8.72 ± 0.06	8.88	8.80	...	8.8 ± 0.16	
41.....	4253	J123638.57+621510.4	0.46196	23.92	23.48	−17.91	0.550	88.5 ± 5.1	18.1 ± 1.4	110.7 ± 4.3	>24.56	0.29	0	0.09	9.91	8.32					

TABLE 1—*Continued*

No.	ID	GOODS ID	$z$	$R$ (mag)	$i_{775W}$ (mag)	$M_B$ (mag)	$U - B$ (mag)	EW				SFR				O/H				
								[O II]	H $\beta$	[O III]	H $\alpha$ /N II	( $M_\odot$ /yr)	CODE	log $O_{32}$	$R_{23}$	M91	KD	Avg.	N II	Final
(1)	(2)	(3)	(4)	(5)	(6)	(7)	(8)	(9)	(10)	(11)	(12)	(13)	(14)	(15)	(16)	(17)	(18)	(19)	(20)	(21)
46.....	2011	J123545.67+621140.0	0.47344	21.61	21.25	-20.30	0.500	$38.6 \pm 1.6$	$11.4 \pm 0.4$	$17.5 \pm 0.7$	...	1.66	0	-0.34	4.18	$8.74 \pm 0.01$	8.91	8.83	...	$8.83 \pm 0.15$
47.....	7557	J123650.22+621240.1	0.47415	21.20	20.75	-20.66	0.610	$31.0 \pm 1.3$	$8.1 \pm 0.4$	$7.7 \pm 0.5$	3.84	1.64	0	-0.6	3.83	$8.76 \pm 0.13$	8.94	8.85	8.77	$8.85 \pm 0.19$
48.....	7992	J123657.30+621300.0	0.47436	22.00	21.39	-19.96	0.530	$54.5 \pm 1.9$	$10.8 \pm 0.6$	$30.4 \pm 0.9$	10.73	1.15	0	-0.25	6.63	$8.52 \pm 0.02$	8.66	8.59	8.51	$8.59 \pm 0.15$
49.....	9087	J123650.74+621059.0	0.47452	21.80	21.34	-20.11	0.590	$56.2 \pm 1.7$	$12.9 \pm 0.8$	$20.0 \pm 0.6$	5.09	1.58	0	-0.44	5.11	$8.65 \pm 0.02$	8.82	8.73	8.73	$8.73 \pm 0.15$
50.....	6912	J123649.37+621311.6	0.47582	22.71	22.20	-19.29	0.580	$57.9 \pm 5.9$	$20.2 \pm 2.0$	$29.0 \pm 2.8$	>4.03	1.16	0	-0.3	3.91	$8.77 \pm 0.04$	8.94	8.85	<8.89	$8.85 \pm 0.15$
51.....	12654	J123730.33+621129.3	0.47646	22.74	22.49	-19.10	0.420	$49.3 \pm 6.3$	$17.5 \pm 1.9$	$67.4 \pm 1.9$	>9.89	0.85	0	0.13	5.98	$8.63 \pm 0.05$	8.76	8.69	<8.7	$8.69 \pm 0.15$
52.....	10829	J123721.77+621225.6	0.47968	22.11	21.63	-19.83	0.710	$26.4 \pm 2.0$	$6.7 \pm 0.4$	$4.8 \pm 0.6$	3.18	0.63	0	-0.73	3.58	$8.78 \pm 0.14$	8.96	8.87	8.79	$8.87 \pm 0.2$
53.....	7572	J123630.26+621014.6	0.48176	22.71	22.30	-19.30	0.650	$42.7 \pm 3.6$	$8.8 \pm 1.0$	$26.8 \pm 1.2$	...	0.51	0	-0.2	6.43	$8.55 \pm 0.05$	8.69	8.62	...	$8.62 \pm 0.15$
54.....	3943	J123623.04+621346.7	0.48446	21.41	20.93	-20.56	0.710	$25.1 \pm 0.5$	$9.2 \pm 0.2$	$6.0 \pm 0.3$	2.83	1.7	0	-0.62	2.77	$8.88 \pm 0.12$	9.03	8.95	8.89	$8.95 \pm 0.19$
55.....	4277	J123726.47+622043.8	0.48524	21.94	21.38	-20.05	0.720	$23.4 \pm 2.4$	$6.4 \pm 0.6$	$7.2 \pm 1.1$	...	0.74	0	-0.51	3.64	$8.79 \pm 0.16$	8.96	8.87	...	$8.87 \pm 0.21$
56.....	1577	J123703.97+622113.3	0.48545	22.94	22.48	-19.16	0.430	$8.7 \pm 0.8$	$4 \pm 0.4$	$12.7 \pm 0.7$	...	0.2	0	0.16	3.56	$8.83 \pm 0.02$	8.97	8.90	...	$8.9 \pm 0.15$
57.....	9034	J123746.17+621731.0	0.48657	22.32	21.79	-19.69	0.790	$40.0 \pm 3.8$	$13 \pm 0.8$	$13.5 \pm 1.2$	...	1.08	0	-0.47	3.56	$8.8 \pm 0.03$	8.97	8.88	...	$8.88 \pm 0.15$
58.....	2568	J123636.15+621657.0	0.48793	21.40	21.05	-20.33	0.580	$41.7 \pm 1.1$	$8.9 \pm 0.5$	$15.3 \pm 0.7$	3.81	1.33	0	-0.43	5.22	$8.64 \pm 0.02$	8.81	8.72	8.84	$8.72 \pm 0.15$
59.....	1226	J123618.89+621621.7	0.50232	22.66	22.24	-19.40	0.460	$70.1 \pm 5.3$	$15.4 \pm 1.6$	$41.9 \pm 2.1$	...	0.98	0	-0.22	6.43	$8.55 \pm 0.05$	8.69	8.62	...	$8.62 \pm 0.15$
60.....	760	J123629.99+621818.2	0.50325	22.08	21.51	-20.02	0.590	$31.9 \pm 1.2$	$11.4 \pm 0.8$	$6.6 \pm 0.7$	4.22	1.28	0	-0.68	2.87	$8.87 \pm 0.14$	9.03	8.95	8.71	$8.95 \pm 0.2$
61.....	4210	J123649.99+621637.4	0.50348	22.12	21.55	-20.04	0.680	$20.2 \pm 1.1$	$7.1 \pm 0.9$	$4.8 \pm 0.5$	...	0.81	0	-0.62	2.74	$8.88 \pm 0.15$	9.03	8.96	...	$8.96 \pm 0.21$
62.....	1987	J123716.20+622214.4	0.50449	22.02	21.49	-20.10	0.720	$21.4 \pm 1.3$	$9 \pm 0.6$	$5.1 \pm 0.4$	...	1.09	0	-0.62	2.40	$8.91 \pm 0.13$	9.06	8.99	...	$8.99 \pm 0.19$
63.....	4192	J123634.27+621448.7	0.50716	23.37	22.91	-18.82	0.410	$51.0 \pm 2.1$	$11.6 \pm 1.2$	$45.6 \pm 1.7$	...	0.43	0	-0.04	7.10	$8.51 \pm 0.05$	8.62	8.57	...	$8.57 \pm 0.15$
64.....	7843	J123615.32+620808.5	0.50858	22.76	22.34	-19.37	0.440	$80.5 \pm 2.1$	$27.4 \pm 1.1$	$109.1 \pm 1.5$	...	1.7	0	0.13	6.44	$8.59 \pm 0.01$	8.71	8.65	...	$8.65 \pm 0.15$
65.....	9435	J123624.64+620727.6	0.50870	21.90	21.52	-20.12	0.610	$38.2 \pm 1.8$	$10.7 \pm 0.6$	$10.6 \pm 0.9$	...	1.32	0	-0.55	3.84	$8.77 \pm 0.13$	8.94	8.85	...	$8.85 \pm 0.19$
66.....	10701	J123732.32+621345.4	0.51011	23.89	23.37	-18.29	0.440	$122.0 \pm 11.5$	$22 \pm 1.8$	$122.5 \pm 2.0$	...	0.5	0	0	10.18	$8.29 \pm 0.06$	8.6	8.45	...	$8.44 \pm 0.16$
67.....	11802	J123746.56+621414.8	0.51130	22.41	21.70	-19.51	0.760	$58.7 \pm 4.2$	$19.7 \pm 2.8$	$32.6 \pm 2.6$	...	1.39	0	-0.25	4.20	$8.75 \pm 0.05$	8.91	8.83	...	$8.83 \pm 0.15$
68.....	6082	J123702.72+621543.9	0.51236	20.34	19.70	-21.57	0.550	$6.1 \pm 0.3$	$2.4 \pm 0.2$	$12.4 \pm 0.2$	...	1.12	0	0.3	4.20	$8.78 \pm 0.01$	8.93	8.86	...	$8.86 \pm 0.15$
69.....	7889	J123617.75+620819.4	0.51241	22.68	22.17	-19.52	0.420	$111.4 \pm 1.8$	$50.4 \pm 1.0$	$178.9 \pm 1.3$	...	3.6	0	0.2	5.54	$8.67 \pm 0.01$	8.81	8.74	...	$8.74 \pm 0.15$
70.....	8749	J123638.20+620953.8	0.51264	21.81	21.24	-20.47	0.550	$43.0 \pm 1.7$	$10.5 \pm 0.8$	$17.5 \pm 0.6$	...	1.79	0	-0.39	4.84	$8.68 \pm 0.03$	8.85	8.76	...	$8.76 \pm 0.15$
71.....	3653	J123650.22+621718.4	0.51283	22.97	22.47	-19.33	0.530	$58.0 \pm 1.4$	$13.6 \pm 0.6$	$40.4 \pm 0.8$	...	0.81	0	-0.15	6.30	$8.57 \pm 0.01$	8.7	8.64	...	$8.64 \pm 0.15$
72.....	2154	J123649.44+621855.8	0.51294	22.84	22.36	-19.36	0.500	$47.7 \pm 2.5$	$12 \pm 1.2$	$25.4 \pm 0.8$	...	0.74	0	-0.27	5.22	$8.65 \pm 0.04$	8.81	8.73	...	$8.73 \pm 0.15$
73.....	10625	J123727.34+621319.2	0.51309	22.44	21.95	-19.69	0.440	$103.2 \pm 2.5$	$48.9 \pm 2.0$	$373.0 \pm 2.9$	...	4.08	0	0.55	9.35	$8.44 \pm 0.01$	8.44	8.44	...	$8.44 \pm 0.15$
74.....	3130	J123655.06+621824.9	0.51604	23.19	22.70	-19.02	0.450	$83.1 \pm 1.6$	$28.2 \pm 1.0$	$184.3 \pm 1.5$	...	1.27	0	0.34	8.85	$8.44 \pm 0.01$	8.47	8.46	...	$8.46 \pm 0.15$
75.....	2470	J123627.73+621602.4	0.51808	23.17	22.69	-19.05	0.550	$58.5 \pm 6.8$	$15.2 \pm 1.9$	$37.2 \pm 4.2$	...	0.7	2	-0.19	5.56	$8.63 \pm 0.06$	8.78	8.70	...	$8.69 \pm 0.16$
76.....	3711	J123633.14+621514.0	0.51962	22.92	22.33	-19.38	0.640	$51.1 \pm 2.3$	$11.7 \pm 1.3$	$21.0 \pm 5.8$	...	0.73	2	-0.38	5.26	$8.63 \pm 0.05$	8.8	8.72	...	$8.72 \pm 0.15$
77.....	8617	J123643.04+621030.7	0.55013	22.47	21.98	-19.84	0.550	$39.1 \pm 3.1$	$12 \pm 1.1$	$19.8 \pm 1.8$	...	1.14	0	-0.29	4.20	$8.74 \pm 0.03$	8.91	8.83	...	$8.83 \pm 0.15$
78.....	8730	J123626.71+620830.1	0.55530	21.54	20.99	-20.62	0.580	$29.7 \pm 1.2$	$7.5 \pm 0.5$	$8.0 \pm 0.7$	...	1.46	0	-0.56	3.96	$8.75 \pm 0.13$	8.93	8.84	...	$8.84 \pm 0.19$
79.....	10183	J123713.00+621209.8	0.55639	23.51	22.9	-18.93	0.570	$85.9 \pm 4.5$	$25 \pm 2.4$	$56.0 \pm 3.1$	...	1.04	0	-0.18	5.25	$8.65 \pm 0.04$	8.81	8.73	...	$8.73 \pm 0.15$
80.....	4231	J123635.40+621450.1	0.55671	23.87	23.43	-18.47	0.530	$47.3 \pm 3.6$	$10 \pm 1.3$	$21.2 \pm 1.7$	...	0.27	0	-0.34	5.70	$8.6 \pm 0.06$	8.76	8.68	...	$8.68 \pm 0.16$
81.....	10113	J123707.79+621138.1	0.55748	23.00	22.48	-19.40	0.420	$70.6 \pm 1.6$	$20.5 \pm 1.0$	$65.2 \pm 1.9$	...	1.31	0	-0.03	6.03	$8.6 \pm 0.02$	8.74	8.67	...	$8.67 \pm 0.15$
82.....	7425	J123718.76+621604.9	0.55766	22.39	21.93	-19.89	0.690	$35.5 \pm 2.1$	$6.7 \pm 0.8$	$22.8 \pm 1.4$	...	0.67	0	-0.19	6.70	$8.53 \pm 0.05$	8.66	8.59	...	$8.59 \pm 0.15$
83.....	8993	J123655.63+621135.8	0.55855	23.00	22.78	-19.14	0.460	$51.4 \pm 3.9$	$16.3 \pm 1.3$	$51.7 \pm 2.7$	...	0.82	0	0	5.63	$8.64 \pm 0.03$	8.79	8.71	...	$8.71 \pm 0.15$
84.....	4191	J123636.29+621501.2	0.55986	23.67	23.18	-18.77	0.460	$27.1 \pm 2.9$	$10.1 \pm 1.6$	$33.5 \pm 2.7$	...	0.36	0	0.09	5.00	$8.71 \pm 0.05$	8.85	8.78	...	$8.77 \pm 0.15$
85.....	10354	J123639.30+620800.1	0.56000	23.78	23.30	-18.57	0.430	$44.4 \pm 5.3$	$7.9 \pm 1.3$	$42.5 \pm 2.7$	...	0.23	0	-0.01	8.77	$8.38 \pm 0.09$	8.44	8.41	...	$8.41 \pm 0.17$
86.....	5668	J123736.93+622009.6	0.58557	23.47	22.82	-19.18	0.610	$55.0 \pm 3.6$	$12.4 \pm 1.2$	$29.9 \pm 4.1$	...	0.64	0	-0.26	5.89	$8.58 \pm 0.04$	8.74	8.66	...	$8.66 \pm 0.15$
87.....	5759	J123736.59+622006.0	0.58570	22.16	21.70	-20.34	0.370	$85.4 \pm 2.2$	$22.3 \pm 1.4$	$43.3 \pm 1.7$	...	3.37	0	-0.29	5.29	$8.64 \pm 0.02$	8.8	8.72	...	$8.72 \pm 0.15$
88.....	5694	J123735.77+622005.7	0.58571	22.40	21.91	-20.09	0.350	$48.5 \pm 2.1$	$31.5 \pm 3.5$	$60.1 \pm 4.2$	...	3.79	0	0.09	3.24	$8.85 \pm 0.03$	8.99	8.92	...	$8.92 \pm 0.15$
89.....	2013	J123707.21+622104.5	0.59430	23.61	23.06	-18.97	0.370	$70.3 \pm 2.9$	$20.3 \pm 1.9$	$40.8 \pm 1.3$	...	0.87	0	-0.23	4.98	$8.68 \pm 0.04$	8.84	8.76	...	$8.76 \pm 0.15$
90.....	9757	J123707.24+621158.1	0.59442	23.11	22.57	-19.45	0.430	$53.4 \pm 1.9$	$11.5 \pm 1.4$	$42.2 \pm 1.4$	...	0.77	0	-0.1	7.08	$8.51 \pm 0.05$	8.62	8.57	...	$8.57 \pm 0.15$
91.....	7887	J123625.01+620913.1	0.59449	22.95	23.25	-18.87	0.460	$143.0 \pm 5.5$	$63.1 \pm 2.5$	$387.2 \pm 2.7$	...	2.48	0</							

TABLE 1—*Continued*

No.	ID	GOODS ID	z	R	i <sub>775W</sub>	M <sub>B</sub>	U - B	EW				SFR				O/H					
				(mag)	(mag)	(mag)	(mag)	[O II]	Hβ	[O III]	Hα/N II	(M <sub>☉</sub> /yr)	CODE	log O <sub>32</sub>	R <sub>23</sub>	M91	KD	Avg.	N II	Final	
(1)	(2)	(3)	(4)	(5)	(6)	(7)	(8)	(9)	(10)	(11)	(12)	(13)	(14)	(15)	(16)	(17)	(18)	(19)	(20)	(21)	
92.....	10248	J123631.67+620714.7	0.59578	22.80	22.33	-19.72	0.580	53.2 ± 2.4	14 ± 1.0	23.4 ± 1.1	...	1.2	0	-0.35	4.78	8.69 ± 0.03	8.85	8.77	...	8.77 ± 0.15	
93.....	10545	J123736.93+621433.4	0.63320	22.12	21.50	-20.55	0.630	30.2 ± 1.3	5.5 ± 0.6	9.0 ± 0.6	...	1.01	0	-0.52	5.22	8.63 ± 0.15	8.8	8.72	...	8.72 ± 0.21	
94.....	8481	J123716.29+621433.0	0.63471	23.16	22.93	-19.34	0.370	61.4 ± 2.8	19.3 ± 2.4	59.6 ± 1.8	...	1.16	0	-0.01	5.68	8.63 ± 0.05	8.78	8.71	...	8.71 ± 0.15	
95.....	3169	J123548.06+621035.1	0.63728	22.08	21.42	-20.71	0.960	33.3 ± 1.4	13.3 ± 0.8	6.5 ± 0.5	...	2.82	0	-0.7	2.60	8.89 ± 0.13	9.05	8.97	...	8.97 ± 0.19	
96.....	2227	J123622.50+621544.8	0.63934	21.07	20.41	-21.60	0.660	15.5 ± 0.9	10.6 ± 0.7	5.1 ± 0.6	...	5.09	0	-0.48	1.63	9.0 ± 0.01	9.11	9.05	...	9.05 ± 0.15	
97.....	1865	J123625.29+621621.9	0.63990	23.69	23.09	-19.17	0.380	50.2 ± 1.8	16.4 ± 1.7	69.3 ± 1.1	...	0.85	0	0.13	6.49	8.58 ± 0.04	8.71	8.64	...	8.64 ± 0.15	
98.....	2841	J123625.44+621519.9	0.64211	22.48	21.97	-20.27	0.430	38.7 ± 1.9	10.3 ± 1.4	24.1 ± 1.5	...	1.46	0	-0.2	5.10	8.67 ± 0.05	8.83	8.75	...	8.75 ± 0.15	
99.....	4375	J123700.52+621733.8	0.66031	23.05	22.38	-19.95	0.390	95.4 ± 2.4	28.6 ± 1.2	100.6 ± 3.1	...	3.03	0	0.02	6.40	8.58 ± 0.01	8.71	8.64	...	8.64 ± 0.15	
100.....	2553	J123646.41+621804.2	0.67301	23.77	23.25	-19.20	0.480	53.2 ± 4.1	18 ± 1.8	47.2 ± 3.2	...	0.95	0	-0.05	5.02	8.68 ± 0.04	8.84	8.76	...	8.76 ± 0.15	
101.....	12739	J123753.22+621417.2	0.67858	23.39	22.84	-19.58	0.310	69.2 ± 2.8	19.8 ± 1.6	110.7 ± 2.9	...	1.49	0	0.2	8.25	8.46 ± 0.04	8.52	8.49	...	8.49 ± 0.15	
102.....	9553	J123648.23+621003.0	0.68064	22.65	22.09	-20.28	0.510	60.3 ± 5.9	13.3 ± 1.8	33.0 ± 4.4	...	1.9	0	-0.26	6.09	8.57 ± 0.07	8.72	8.65	...	8.65 ± 0.16	
103.....	5619	J123712.00+621727.4	0.68069	22.25	21.68	-20.67	0.490	49.1 ± 2.6	10.1 ± 1.5	30.3 ± 2.5	...	2.07	0	-0.2	6.56	8.54 ± 0.07	8.67	8.61	...	8.61 ± 0.16	
104.....	5312	J123735.55+622030.7	0.68131	22.73	22.07	-20.31	0.570	31.1 ± 2.3	7 ± 0.5	6.6 ± 1.9	...	1.03	0	-0.67	4.18	8.72 ± 0.16	8.91	8.81	...	8.81 ± 0.21	
105.....	2644	J123624.31+621525.6	0.68166	23.49	22.59	-19.77	0.930	14.8 ± 2.1	6.5 ± 0.9	4.7 ± 1.6	...	0.58	0	-0.49	2.29	8.93 ± 0.04	9.07	9.00	...	9 ± 0.15	
106.....	2514	J123638.74+621706.8	0.68209	22.25	21.67	-20.73	0.600	38.9 ± 1.0	12.9 ± 0.4	17.0 ± 1.4	...	2.79	0	-0.35	3.75	8.79 ± 0.01	8.95	8.87	...	8.87 ± 0.15	
107.....	8938	J123649.95+621059.1	0.68313	23.41	22.55	-19.83	0.630	35.9 ± 2.7	5.7 ± 0.9	10.7 ± 1.1	...	0.54	0	-0.52	6.05	8.54 ± 0.20	8.71	8.63	...	8.63 ± 0.25	
108.....	1953	J123613.72+621453.3	0.68536	23.97	23.46	-19.08	0.340	91.4 ± 9.1	38.4 ± 2.7	197.3 ± 16.9	...	1.83	0	0.33	7.14	8.56 ± 0.04	8.65	8.61	...	8.61 ± 0.15	
109.....	8190	J123724.53+621547.4	0.69101	22.75	22.11	-20.32	0.490	57.1 ± 2.9	13.9 ± 1.1	26.2 ± 1.8	...	2.06	0	-0.33	5.23	8.65 ± 0.03	8.81	8.73	...	8.73 ± 0.15	
110.....	4389	J123619.85+621252.0	0.69442	21.15	20.58	-21.84	0.410	59.8 ± 0.9	28.4 ± 0.8	102.0 ± 0.8	...	17.0	0	0.23	5.32	8.69 ± 0.01	8.83	8.76	...	8.76 ± 0.15	
111.....	4712	J123642.73+621503.2	0.69731	24.02	23.15	-19.43	0.610	55.1 ± 4.6	10.2 ± 1.7	14.3 ± 1.8	...	0.67	0	-0.58	5.68	8.57 ± 0.21	8.75	8.66	...	8.66 ± 0.25	
112.....	8126	J123720.58+621520.1	0.69780	23.69	23.08	-19.46	0.360	71.6 ± 4.4	24.2 ± 1.9	95.1 ± 3.3	...	1.63	0	0.12	6.36	8.59 ± 0.03	8.72	8.65	...	8.65 ± 0.15	
113.....	13234	J123703.93+620841.9	0.70356	22.88	22.36	-20.17	0.390	64.9 ± 5.1	19.3 ± 1.8	101.5 ± 2.6	...	2.5	0	0.19	7.81	8.49 ± 0.05	8.57	8.53	...	8.52 ± 0.15	
114.....	13683	J123701.49+620842.4	0.70376	22.16	21.43	-20.98	0.630	26.7 ± 1.1	9.4 ± 0.3	5.5 ± 0.6	...	2.56	0	-0.68	2.82	8.87 ± 0.13	9.03	8.95	...	8.95 ± 0.19	
115.....	3738	J123730.26+622130.2	0.70781	22.40	21.77	-20.56	0.470	78.2 ± 2.4	13.4 ± 1.5	35.3 ± 2.2	...	2.48	0	-0.34	7.37	8.45 ± 0.05	8.57	8.51	...	8.51 ± 0.15	
116.....	5167	J123702.48+621645.5	0.74411	24.06	23.47	-19.34	0.390	98.9 ± 7.0	38.9 ± 5.2	108.4 ± 3.7	...	2.35	0	0.03	5.06	8.69 ± 0.06	8.84	8.77	...	8.77 ± 0.16	
117.....	7818	J123703.83+621353.8	0.74502	22.46	21.99	-20.66	0.420	61.7 ± 2.0	13.1 ± 0.5	45.7 ± 0.9	...	2.66	0	-0.13	7.11	8.49 ± 0.01	8.62	8.56	...	8.56 ± 0.15	
118.....	6988	J123618.63+620933.6	0.74729	22.45	21.65	-20.93	0.580	35.0 ± 1.8	7 ± 1.0	13.7 ± 1.0	...	1.82	0	-0.4	5.41	8.62 ± 0.06	8.79	8.70	...	8.69 ± 0.16	
119.....	1432	J123604.13+621425.2	0.74789	23.14	22.54	-20.23	0.590	45.8 ± 3.5	15.8 ± 1.7	23.6 ± 2.3	...	2.16	0	-0.28	3.89	8.77 ± 0.04	8.94	8.86	...	8.86 ± 0.15	
120.....	3405	J123558.10+621131.9	0.74799	23.53	22.79	-19.96	0.550	49.4 ± 3.2	7.9 ± 0.9	8.1 ± 0.9	...	0.84	0	-0.78	5.80	8.54 ± 0.17	8.73	8.63	...	8.63 ± 0.22	
121.....	7872	J123614.83+620801.1	0.74806	23.27	22.73	-20.04	0.590	46.7 ± 2.1	16.6 ± 1.8	69.6 ± 3.6	...	1.91	0	0.17	6.25	8.61 ± 0.04	8.73	8.67	...	8.67 ± 0.15	
122.....	11299	J123701.99+620939.3	0.74985	23.16	22.68	-20.07	0.530	72.0 ± 4.1	19.7 ± 2.2	32.6 ± 3.2	...	2.33	0	-0.34	4.82	8.68 ± 0.05	8.85	8.77	...	8.77 ± 0.15	
123.....	8720	J123715.71+621417.0	0.76093	22.82	22.01	-20.68	0.610	36.6 ± 2.0	11.7 ± 1.6	29.1 ± 2.9	...	2.42	0	-0.09	4.79	8.7 ± 0.05	8.86	8.78	...	8.77 ± 0.15	
124.....	6570	J123659.92+621450.3	0.76101	22.38	21.58	-21.17	0.730	36.4 ± 1.5	14 ± 1.0	13.2 ± 1.9	...	4.53	0	-0.44	3.10	8.85 ± 0.02	9.01	8.93	...	8.93 ± 0.15	
125.....	4794	J123629.67+621325.3	0.76122	24.10	23.30	-19.46	0.390	75.3 ± 2.0	22 ± 1.7	100.0 ± 4.0	...	1.48	0	0.12	7.30	8.52 ± 0.03	8.62	8.57	...	8.57 ± 0.15	
126.....	6157	J123624.02+621110.2	0.76543	23.27	22.4	-20.40	0.680	40.1 ± 2.6	16 ± 2.2	38.7 ± 4.2	...	2.56	0	-0.01	4.37	8.75 ± 0.05	8.9	8.82	...	8.82 ± 0.15	
127.....	9720	J123636.85+620829.6	0.76557	23.57	22.81	-19.86	0.570	55.0 ± 2.7	12.4 ± 1.4	23.7 ± 2.8	...	1.21	0	-0.36	5.46	8.62 ± 0.04	8.78	8.70	...	8.69 ± 0.15	
128.....	11370	J123711.61+621042.8	0.77781	22.76	22.11	-20.74	0.470	54.4 ± 1.2	19.1 ± 1.8	41.8 ± 2.7	...	4.17	0	-0.11	4.55	8.73 ± 0.03	8.88	8.81	...	8.81 ± 0.15	
129.....	2681	J123612.30+621355.4	0.78192	24.31	23.51	-19.41	0.660	59.4 ± 2.3	20.9 ± 2.3	61.2 ± 2.7	...	1.35	0	0.01	5.26	8.67 ± 0.04	8.82	8.75	...	8.75 ± 0.15	
130.....	10713	J123711.39+621122.5	0.78426	23.85	22.80	-20.01	0.730	64.1 ± 4.4	9.4 ± 1.2	13.9 ± 3.0	...	1.05	0	-0.66	6.84	8.45 ± 0.19	8.61	8.53	...	8.52 ± 0.24	
131.....	8745	J123708.36+621321.0	0.78755	23.54	22.85	-20.04	0.510	50.4 ± 2.7	12.3 ± 1.3	28.1 ± 1.7	...	1.41	0	-0.25	5.48	8.63 ± 0.04	8.79	8.71	...	8.71 ± 0.15	
132.....	3173	J123708.53+622001.0	0.78871	23.33	22.66	-20.29	0.550	37.7 ± 1.3	11.7 ± 0.9	17.9 ± 2.2	...	1.69	0	-0.32	4.05	8.76 ± 0.02	8.92	8.84	...	8.84 ± 0.15	
133.....	4628	J123705.27+621746.7	0.78879	23.98	23.25	-19.76	0.500	70.7 ± 3.2													

TABLE 1—*Continued*

No.	ID	GOODS ID	z	R	i <sub>775W</sub>	M <sub>B</sub>	U − B	EW				SFR				O/H					
				(mag)	(mag)	(mag)	(mag)	[O II]	Hβ	[O III]	Hα/N II	(M <sub>☉</sub> /yr)	CODE	log O <sub>32</sub>	R <sub>23</sub>	M91	KD	Avg.	N II	Final	
(1)	(2)	(3)	(4)	(5)	(6)	(7)	(8)	(9)	(10)	(11)	(12)	(13)	(14)	(15)	(16)	(17)	(18)	(19)	(20)	(21)	
138.....	4008	J123558.91+621048.3	0.79709	23.43	22.63	−20.27	0.580	35.3 ± 2.4	10.4 ± 1.2	10.5 ± 1.3	...	1.47	0	−0.52	3.69	8.78 ± 0.16	8.95	8.87	...	8.87 ± 0.21	
139.....	2968	J123619.40+621429.1	0.79740	23.41	22.53	−20.41	0.630	19.6 ± 1.3	8.7 ± 0.8	9.8 ± 1.4	...	1.4	0	−0.3	2.74	8.89 ± 0.02	9.03	8.96	...	8.96 ± 0.15	
140.....	1468	J123618.46+621601.9	0.79803	23.18	22.67	−20.34	0.470	88.7 ± 3.5	42.3 ± 2.7	142.2 ± 4.0	...	6.4	0	0.2	5.21	8.7 ± 0.01	8.84	8.77	...	8.77 ± 0.15	
141.....	5730	J123606.99+620937.2	0.79834	23.18	22.45	−20.51	0.600	39.5 ± 1.8	11.3 ± 1.3	30.9 ± 2.0	...	2.0	0	−0.1	5.29	8.66 ± 0.04	8.81	8.74	...	8.74 ± 0.15	
142.....	10518	J123629.54+620646.9	0.79839	21.52	20.79	−22.07	0.590	25.0 ± 0.9	14.3 ± 0.6	8.9 ± 1.0	...	10.5	0	−0.44	2.07	8.96 ± 0.01	9.08	9.02	...	9.02 ± 0.15	
143.....	6754	J123744.62+621945.5	0.79988	23.72	23.04	−19.93	0.460	48.3 ± 3.8	14.7 ± 1.6	30.4 ± 2.2	...	1.52	0	−0.2	4.71	8.7 ± 0.05	8.87	8.78	...	8.77 ± 0.15	
144.....	9785	J123700.76+621107.5	0.80031	23.63	22.85	−20.09	0.580	52.3 ± 2.6	19.3 ± 1.2	31.2 ± 1.6	...	2.32	0	−0.22	3.92	8.78 ± 0.01	8.94	8.86	...	8.86 ± 0.15	
145.....	10462	J123634.41+620719.0	0.80127	23.05	22.35	−20.63	0.640	39.8 ± 2.3	6.9 ± 0.7	8.1 ± 2.0	...	1.36	0	−0.69	5.38	8.59 ± 0.17	8.78	8.68	...	8.68 ± 0.22	
146.....	3186	J123617.57+621402.5	0.81659	22.49	21.88	−21.09	0.430	55.3 ± 0.9	22.6 ± 0.9	43.2 ± 0.7	...	6.8	0	−0.1	4.00	8.77 ± 0.01	8.93	8.85	...	8.85 ± 0.15	
147.....	11643	J123714.14+621044.8	0.82058	23.15	22.59	−20.44	0.390	103.9 ± 1.2	28.2 ± 1.0	130.1 ± 0.9	...	4.68	0	0.09	7.74	8.49 ± 0.01	8.57	8.53	...	8.52 ± 0.15	
148.....	10478	J123739.17+621454.9	0.82068	21.96	21.28	−21.74	0.610	44.3 ± 1.4	10.6 ± 0.7	12.9 ± 0.9	...	5.79	0	−0.53	4.53	8.7 ± 0.14	8.87	8.78	...	8.77 ± 0.2	
149.....	12095	J123713.82+621038.0	0.82167	23.92	23.27	−19.82	0.400	41.0 ± 3.8	13.9 ± 1.2	105.7 ± 1.8	...	1.3	0	0.41	9.22	8.43 ± 0.04	8.43	8.43	...	8.43 ± 0.15	
150.....	4332	J123650.64+621629.3	0.83567	24.01	23.4	−19.68	0.460	91.4 ± 3.2	30.5 ± 2.9	113.5 ± 2.6	...	2.52	0	0.09	6.30	8.6 ± 0.04	8.72	8.66	...	8.66 ± 0.15	
151.....	3021	J123705.47+621951.2	0.83571	22.97	22.29	−20.80	0.540	86.1 ± 1.6	33 ± 2.9	104.0 ± 1.9	...	7.62	0	0.08	5.43	8.66 ± 0.03	8.81	8.74	...	8.74 ± 0.15	
152.....	7072	J123708.37+621515.0	0.83920	22.40	21.63	−21.48	0.550	35.8 ± 2.3	9.5 ± 1.2	17.7 ± 1.7	...	4.09	0	−0.3	4.65	8.7 ± 0.05	8.87	8.79	...	8.79 ± 0.15	
153.....	6865	J123706.58+621513.5	0.83937	24.07	23.64	−19.50	0.520	67.5 ± 3.7	13.9 ± 1.8	57.8 ± 3.8	...	0.97	0	−0.06	7.88	8.45 ± 0.07	8.53	8.49	...	8.49 ± 0.16	
154.....	6786	J123706.31+621518.4	0.83977	22.52	22.00	−21.10	0.420	52.5 ± 2.0	25.2 ± 1.6	74.1 ± 1.9	...	7.66	0	0.14	4.65	8.74 ± 0.01	8.89	8.81	...	8.81 ± 0.15	
155.....	7075	J123714.06+621549.6	0.83987	24.00	23.48	−19.66	0.420	86.9 ± 6.6	29.7 ± 2.6	133.4 ± 2.9	...	2.41	0	0.18	6.94	8.55 ± 0.03	8.66	8.61	...	8.61 ± 0.15	
156.....	5707	J123608.31+620952.2	0.84029	22.99	22.11	−20.94	0.580	27.5 ± 2.1	14.2 ± 1.8	11.3 ± 1.8	...	3.72	0	−0.38	2.39	8.93 ± 0.03	9.06	8.99	...	8.99 ± 0.15	
157.....	9067	J123713.11+621334.1	0.84072	22.93	22.27	−20.80	0.500	45.0 ± 2.5	16.8 ± 1.6	24.5 ± 2.0	...	3.87	0	−0.26	3.69	8.8 ± 0.03	8.96	8.88	...	8.88 ± 0.15	
158.....	9211	J123727.59+621459.3	0.84092	23.81	23.09	−20.04	0.500	58.5 ± 4.0	31.3 ± 3.1	91.0 ± 4.5	...	3.6	0	0.19	4.48	8.75 ± 0.03	8.9	8.83	...	8.83 ± 0.15	
159.....	7400	J123627.22+621002.4	0.84142	22.52	21.87	−21.24	0.500	38.7 ± 0.0	14.4 ± 1.3	16.8 ± 0.9	...	4.97	0	−0.36	3.38	8.83 ± 0.02	8.98	8.90	...	8.9 ± 0.15	
160.....	7878	J123719.17+621530.4	0.84173	23.54	23.02	−20.06	0.390	107.5 ± 6.6	54.4 ± 4.0	131.4 ± 4.3	...	6.37	0	0.08	4.23	8.77 ± 0.02	8.92	8.84	...	8.84 ± 0.15	
161.....	8109	J123643.97+621107.4	0.84532	23.77	22.95	−20.25	0.470	46.1 ± 2.2	16.1 ± 1.4	88.6 ± 1.6	...	2.24	0	0.28	7.44	8.53 ± 0.03	8.62	8.57	...	8.57 ± 0.15	
162.....	3139	J123617.58+621408.6	0.84612	23.25	22.86	−20.30	0.560	39.2 ± 2.3	10.9 ± 1.2	22.7 ± 1.8	...	1.59	0	−0.23	4.79	8.69 ± 0.04	8.86	8.77	...	8.77 ± 0.15	
163.....	5627	J123654.15+621515.4	0.84876	23.40	22.78	−20.40	0.440	90.4 ± 6.7	19.8 ± 1.7	51.5 ± 2.8	...	3.16	0	−0.24	6.50	8.53 ± 0.05	8.68	8.61	...	8.61 ± 0.15	
164.....	1890	J123617.33+621530.0	0.84975	22.35	21.46	−21.70	0.750	12.0 ± 1.4	8.5 ± 1.0	3.2 ± 1.1	...	4.47	0	−0.57	1.44	9.02 ± 0.14	9.12	9.07	...	9.07 ± 0.2	
165.....	4888	J123653.93+621607.3	0.84991	23.48	22.74	−20.45	0.490	69.0 ± 2.0	16.6 ± 0.8	54.7 ± 1.1	...	2.78	0	−0.1	6.65	8.54 ± 0.02	8.67	8.60	...	8.6 ± 0.15	
166.....	8579	J123712.66+621357.6	0.85018	23.89	23.13	−20.02	0.520	47.0 ± 3.6	15.5 ± 1.7	46.7 ± 2.7	...	1.75	0	0	5.35	8.67 ± 0.04	8.81	8.74	...	8.74 ± 0.15	
167.....	8349	J123724.08+621535.9	0.85070	22.95	22.29	−20.75	0.450	53.0 ± 3.2	16 ± 1.3	29.4 ± 2.0	...	3.52	0	−0.25	4.57	8.71 ± 0.03	8.88	8.79	...	8.79 ± 0.15	
168.....	4780	J123646.23+621527.6	0.85097	22.87	22.00	−21.00	0.700	54.0 ± 2.6	14 ± 1.6	15.4 ± 1.5	...	3.88	0	−0.54	4.33	8.72 ± 0.16	8.89	8.80	...	8.8 ± 0.21	
169.....	6596	J123715.45+621632.9	0.85182	23.37	22.59	−20.50	0.500	32.2 ± 2.9	23 ± 2.9	28.1 ± 2.5	...	4.03	0	−0.05	2.41	8.93 ± 0.02	9.05	8.99	...	8.99 ± 0.15	
170.....	3718	J123630.84+621453.9	0.86408	24.00	23.36	−19.84	0.440	86.5 ± 2.3	19.9 ± 1.3	48.8 ± 1.8	...	1.9	0	−0.24	6.17	8.56 ± 0.02	8.71	8.64	...	8.64 ± 0.15	
171.....	8020	J123640.89+621055.1	0.87360	23.28	22.52	−20.68	0.480	45.2 ± 1.5	11.5 ± 0.6	40.0 ± 3.3	...	2.37	2	−0.05	6.31	8.58 ± 0.02	8.71	8.65	...	8.65 ± 0.15	
172.....	2882	J123658.97+621916.3	0.87506	23.61	23.07	−20.10	0.330	68.8 ± 2.8	49.8 ± 3.1	168.0 ± 6.7	...	6.05	0	0.38	4.57	8.77 ± 0.01	8.9	8.83	...	8.83 ± 0.15	
173.....	4003	J123659.54+621758.7	0.90479	22.55	21.71	−21.47	0.470	33.9 ± 1.2	15.8 ± 1.8	14.7 ± 2.5	...	6.74	0	−0.36	2.73	8.89 ± 0.03	9.03	8.96	...	8.96 ± 0.15	
174.....	10529	J123706.34+621057.8	0.90573	24.14	23.32	−19.98	0.490	81.8 ± 4.6	15.3 ± 1.5	39.7 ± 4.5	...	1.66	0	−0.31	7.02	8.48 ± 0.05	8.61	8.55	...	8.55 ± 0.15	
175.....	10350	J123708.68+621128.7	0.90716	22.89	22.4	−20.86	0.330	110.2 ± 2.3	50.7 ± 1.9	173.0 ± 2.8	...	12.3	0	0.19	5.37	8.69 ± 0.01	8.82	8.75	...	8.75 ± 0.15	
176.....	10409	J123753.09+621632.0	0.91295	23.19	22.22	−20.92	0.340	80.3 ± 2.7	15.8 ± 2.6	45.7 ± 2.7	...	4.07	0	−0.24	7.07	8.49 ± 0.08	8.61	8.55	...	8.55 ± 0.17	
177.....	10399	J123642.42+620822.1	0.93610	23.23	22.55	−20.94	0.550	71.9 ± 1.5	16.5 ± 1.4	41.3 ± 2.1	...	4.33	0	−0.24	6.11	8.57 ± 0.03	8.72	8.65	...	8.65 ± 0.15	
178.....	5379	J123704.63+621652.1	0.37657	20.93	20.44	−20.12	0.730	12.0 ± 1.3	5.8 ± 0.4	10.8 ± 0.0	3.11	0.71	3	−0.04	2.92	>8.88	>9.01	>8.95	9.11	>8.95	

TABLE 1—*Continued*

No.	ID	GOODS ID	$z$	$R$	$i_{775W}$	$M_B$	$U - B$	EW				SFR	CODE	$\log O_{32}$	$R_{23}$	O/H				
				(mag)	(mag)	(mag)	(mag)	[O II]	H $\beta$	[O III]	H $\alpha$ /N II	( $M_\odot$ /yr)				M91	KD	Avg.	N II	Final
(1)	(2)	(3)	(4)	(5)	(6)	(7)	(8)	(9)	(10)	(11)	(12)	(13)	(14)	(15)	(16)	(17)	(18)	(19)	(20)	(21)
184.....	10106	J123648.63+620932.6	0.51770	21.74	21.23	-20.31	0.670	46.9 $\pm$ 2.2	9 $\pm$ 0.8	11.1 $\pm$ 0.0	...	1.32	3	-0.62	5.27	>8.61	>8.79	>8.70	...	>8.69
185.....	6623	J123651.79+621354.2	0.55607	21.85	21.20	-20.50	0.780	17.1 $\pm$ 1.4	6.8 $\pm$ 0.9	18.0 $\pm$ 0.0	...	1.19	3	0.02	3.98	>8.78	>8.94	>8.86	...	>8.86
186.....	5038	J123626.61+621252.4	0.55653	21.41	20.79	-20.82	0.640	15.1 $\pm$ 0.9	4.2 $\pm$ 0.5	9.4 $\pm$ 0.0	...	0.98	3	-0.2	3.95	>8.78	>8.94	>8.86	...	>8.86
187.....	10712	J123634.85+620710.5	0.63442	21.55	20.85	-21.26	0.740	8.1 $\pm$ 1.1	8.3 $\pm$ 0.7	6.7 $\pm$ 0.0	...	2.92	3	-0.08	1.43	>9.02	>9.1	>9.06	...	>9.06
188.....	11074	J123747.37+621513.1	0.67897	21.80	21.08	-21.21	0.730	13.6 $\pm$ 2.0	5.8 $\pm$ 0.5	14.7 $\pm$ 0.0	...	1.95	3	0.03	3.62	>8.82	>8.97	>8.89	...	>8.89
189.....	432	J123636.09+621905.6	0.68091	22.60	21.80	-20.54	0.740	14.5 $\pm$ 2.3	8.2 $\pm$ 1.2	33.1 $\pm$ 0.0	...	1.49	3	0.35	4.66	>8.76	>8.89	>8.82	...	>8.82
190.....	4427	J123621.57+621300.7	0.68814	21.91	21.13	-21.16	0.730	13.1 $\pm$ 1.6	7.2 $\pm$ 0.6	50.4 $\pm$ 0.0	...	2.31	3	0.58	6.90	>8.62	>8.7	>8.66	...	>8.66
191.....	5223	J123608.00+621026.1	0.74687	22.38	21.56	-21.07	0.770	23.3 $\pm$ 2.3	7.1 $\pm$ 1.4	40.3 $\pm$ 0.0	...	2.09	3	0.23	6.98	>8.56	>8.66	>8.61	...	>8.61
192.....	8436	J123706.21+621333.1	0.75236	22.63	21.85	-20.71	0.710	16.4 $\pm$ 2.0	7 $\pm$ 1.3	27.2 $\pm$ 0.0	...	1.48	3	0.21	4.84	>8.73	>8.87	>8.80	...	>8.8
193.....	8566	J123705.83+621317.5	0.75293	22.87	22.03	-20.56	0.610	38.7 $\pm$ 2.6	10.8 $\pm$ 1.6	58.6 $\pm$ 0.0	...	2.0	3	0.18	7.60	>8.5	>8.59	>8.54	...	>8.54
194.....	3789	J123629.90+621441.3	0.76096	23.44	22.50	-20.26	0.770	16.2 $\pm$ 1.7	5.8 $\pm$ 1.0	29.7 $\pm$ 0.0	...	0.81	3	0.26	5.88	>8.65	>8.78	>8.71	...	>8.71
195.....	2884	J123631.65+621604.4	0.78374	22.23	21.4	-21.46	0.720	19.5 $\pm$ 0.7	7.4 $\pm$ 0.4	8.9 $\pm$ 0.0	...	3.12	3	-0.34	3.02	>8.86	>9.01	>8.94	...	>8.94
196.....	8013	J123707.43+621357.0	0.78803	24.16	23.34	-19.57	0.590	45.1 $\pm$ 4.1	20.9 $\pm$ 3.3	38.0 $\pm$ 0.0	...	1.56	3	-0.07	3.62	>8.82	>8.96	>8.89	...	>8.89
197.....	8895	J123722.21+621449.4	0.79687	22.58	21.73	-21.21	0.750	14.3 $\pm$ 1.4	8.1 $\pm$ 1.1	15.7 $\pm$ 0.0	...	2.72	3	0.04	2.97	>8.88	>9.01	>8.94	...	>8.94
198.....	5292	J123633.59+621320.2	0.84455	22.43	21.53	-21.60	0.730	6.2 $\pm$ 1.2	4.3 $\pm$ 0.9	10.1 $\pm$ 0.0	...	2.06	3	0.21	2.58	>8.92	>9.03	>8.97	...	>8.97
199.....	4238	J123608.13+621140.8	0.88751	22.95	22.33	-20.76	0.490	37.7 $\pm$ 2.5	12.7 $\pm$ 1.6	47.4 $\pm$ 0.0	...	2.82	3	0.09	5.78	>8.63	>8.78	>8.70	...	>8.69
200.....	8698	J123644.40+621037.3	0.88887	23.63	22.64	-20.50	0.490	44.0 $\pm$ 2.9	15.1 $\pm$ 2.5	112.5 $\pm$ 0.0	...	2.64	3	0.4	9.15	>8.43	>8.44	>8.43	...	>8.43
201.....	10862	J123730.89+621328.3	0.89032	23.20	22.49	-20.83	0.630	34.2 $\pm$ 1.6	11.5 $\pm$ 1.8	81.7 $\pm$ 0.0	...	2.72	3	0.37	8.58	>8.46	>8.5	>8.48	...	>8.48
202.....	9627	J123716.72+621310.5	0.89883	23.33	22.56	-20.80	0.610	34.2 $\pm$ 1.8	11.4 $\pm$ 0.7	32.5 $\pm$ 0.0	...	2.63	3	-0.02	4.97	>8.7	>8.85	>8.77	...	>8.77
203.....	9727	J123705.87+621154.0	0.90316	21.89	21.03	-22.23	0.710	19.7 $\pm$ 1.4	9.9 $\pm$ 0.9	24.4 $\pm$ 0.0	...	8.47	3	0.09	3.70	>8.82	>8.96	>8.89	...	>8.89
204.....	10137	J123719.60+621256.5	0.90890	23.88	22.87	-20.57	0.780	21.4 $\pm$ 1.7	7.8 $\pm$ 1.0	46.3 $\pm$ 0.0	...	1.45	3	0.33	6.90	>8.58	>8.68	>8.63	...	>8.63

NOTES.—Col. (1): Reference ID number for this paper; col. (2): TKRS ID (Wirth et al. 2004); col. (3): GOODS-N Version 1.0 catalog identifier; col. (4): spectroscopic redshift (Wirth et al. 2004); col. (5): TKRS  $R$ -band magnitude; col. (6): GOODS-N Version 1.0 catalog  $i$ -band F775W magnitude; col. (7): rest-frame  $M_B$  for  $H_0 = 70 \text{ km s}^{-1} \text{ Mpc}^{-1}$ ,  $\Omega_M = 0.3$ , and  $\Omega_\Lambda = 0.7$ ; col. (8): rest-frame  $U - B$  color; col. (9): measured EW of [O II]  $\lambda 3727$  and uncertainty, corrected to the rest frame; col. (10): measured EW of H $\beta$   $\lambda 4861$  and uncertainty, corrected to the rest frame (no correction for stellar absorption); col. (11): measured EW of [O III]  $\lambda 4959 + \lambda 5007$  determined from  $1.3W_{[\text{O III}]\lambda 5007}$  and uncertainty, corrected to the rest frame; col. (12): measured EW ratio of H $\alpha$ /[N II]  $\lambda 6584$  corrected to the rest frame; col. (13): estimated SFR based on H $\beta$  flux (not corrected for stellar absorption), derived from the EW(H $\beta$ ) and  $B$ -band absolute magnitude. We estimate the H $\beta$  luminosity as  $L_{\text{H}\beta}(\text{ergs s}^{-1}) = 5.49 \times 10^{31} \times 2.5^{-M_B} \text{EW}_{\text{H}\beta}$ . The SFR is then computed by  $\text{SFR}(M_\odot \text{ yr}^{-1}) = 2.8L_{\text{H}\beta}/1.26 \times 10^{41}$ , which assumes the Kennicutt (1998) calibration of SFR in terms of H $\alpha$  luminosity. This estimate is a lower limit, since dust extinction and stellar Balmer absorption are not taken into account; col. (14): Code: 0 = oxygen abundance computed using  $\text{EWR}_{23} = (W_{[\text{O II}]\lambda 3727} + 1.3W_{[\text{O III}]\lambda 5007})/W_{\text{H}\beta}$ ; 1 = object is probably on the turnaround region of the  $R_{23}$ -O/H calibration or possibly on the lower branch based on the [N II]  $\lambda 6584/\text{H}\alpha$  ratio, so the lower branch formula of McGaugh (1991) is applied and averaged with the upper branch estimate of KD02 to arrive at the oxygen abundance in col. (19); 2 = oxygen abundance computed using  $\text{EWR}_{23} = (W_{[\text{O II}]\lambda 3727} + 4W_{[\text{O III}]\lambda 4959})/W_{\text{H}\beta}$ ; 3 =  $W_{[\text{O III}]\lambda 5007}$  is measured with S/N less than 3:1 so a  $3\sigma$  lower limit on the oxygen abundance is computed using  $\text{EWR}_{23} = (W_{[\text{O II}]\lambda 3727} + 1.3W_{[\text{O III}]\lambda 5007})/W_{\text{H}\beta}$ ; col. (15):  $\log O_{32} = 1.3W_{[\text{O III}]\lambda 5007}/W_{[\text{O II}]\lambda 3727}$ ; col. (16):  $R_{23} = \text{EWR}_{23} = (W_{[\text{O II}]\lambda 3727} + 1.3W_{[\text{O III}]\lambda 5007})/W_{\text{H}\beta}$ ; col. (17): oxygen abundance,  $12 + \log(\text{O}/\text{H})$ , and  $1\sigma$  uncertainty from the empirical  $R_{23}$  method following McGaugh (1991) as formulated in KKP99 after correction for  $2\text{ \AA}$  of stellar absorption in the EW $_{\text{H}\beta}$ . The uncertainty reflects the statistical measurement error on the line EWs only and does not include systematic uncertainties in the calibration method, which may exceed 0.1 dex in  $12 + \log(\text{O}/\text{H})$ ; col. (18): oxygen abundance,  $12 + \log(\text{O}/\text{H})$  based on the  $\text{EWR}_{23}$  and the models of Kewley & Dopita (2003) as given in equations in the text; col. (19): mean of oxygen abundances from cols. (17) and (18); col. (20): oxygen abundance estimated using  $O_{32}$  and the [N II]/H $\alpha$  ratio in conjunction with the photoionization models and parametric relations of eqs. (12) and (13); col. (21): final adopted best estimate oxygen abundance. This is simply the value from col. (19) in most cases. For objects with code = 1 that are on the lower branch or turnaround region of the  $R_{23}$ -O/H calibration, this value is the average of cols. (17) and (18). See text and Garnett et al. (2004) for possible systematic uncertainties in the absolute metallicities, which may reach 0.2–0.5 dex, particularly in metal-rich systems. Table 1 is also available in machine-readable form in the electronic edition of the *Astrophysical Journal*.

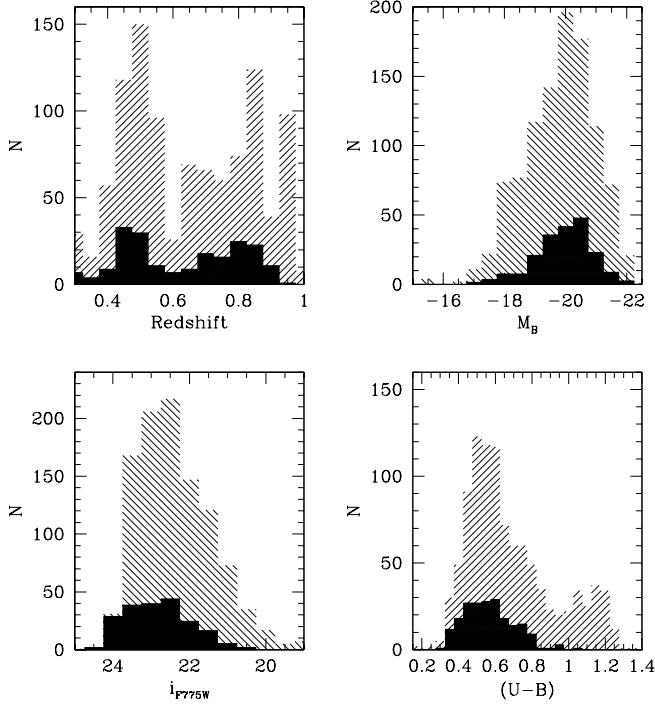


FIG. 1.—Histogram of 204 galaxies selected for chemical analysis (*large symbols*) compared with the total 1044 objects in the TKRS survey with spectroscopic redshifts  $0.3 < z < 1.0$ . We show the distribution as a function of redshift, observed  $i$ -band magnitude,  $M_B$ , and  $U - B$  color. This figure demonstrates that galaxies selected as suitable for chemical analysis are reasonably representative of the larger TKRS sample in the GOODS-N field in terms of their redshift distributions, magnitudes, and luminosities. However, the 204 selected galaxies preferentially have bluer  $U - B$  colors consistent with higher rates of star formation, and they comprise a disproportionate fraction of galaxies near the faint end of the survey limit at  $R \sim 24$ .

show the redshift distribution,  $z$ , the absolute  $B$  magnitudes,  $M_B$ , the observed  $i$ -band (F774W) magnitudes, and the rest-frame colors,  $(U - B)$ . Shaded histograms denote the selected objects, while hatched histograms show the entire TKRS sample of 1044 objects. Examination of Figure 1 reveals that the 204 galaxies selected for chemical analysis are representative of the entire TKRS sample in terms of their blue luminosities and redshift distribution. The lower left panel indicates that the faintest galaxies in the survey, those near the cutoff limit, tend to be preferentially selected by our criteria. The lower right panel indicates that our selection criteria also choose preferentially the bluest galaxies in the TKRS. This disproportionate fraction of blue galaxies is consistent with our emission-line criteria. Those galaxies undergoing strong episodes of star formation will have the bluest colors and will necessarily be the ones with nebular  $H\beta$ ,  $[O II]$ , and  $[O III]$  emission lines.

Figure 2 shows this selection in a slightly different way, plotting redshift,  $z$ , versus photometric properties  $M_B$ ,  $(U - B)$ , and  $i$ -band magnitude. Small dots indicate the whole set of 1044 TKRS galaxies in the range  $0.3 < z < 1.0$ , and filled symbols show just the 204 selected galaxies. This figure shows that, at any given redshift, the objects chosen for chemical analysis are representative of the distribution of  $i$ -band magnitudes of  $M_B$ . The middle panel of Figure 2 shows that the selected galaxies preferentially fall among the bluest half of the TKRS sample, for the reasons mentioned above. Thus, it is important to emphasize that this study is sensitive to the evolution of the chemical and luminous properties of only the

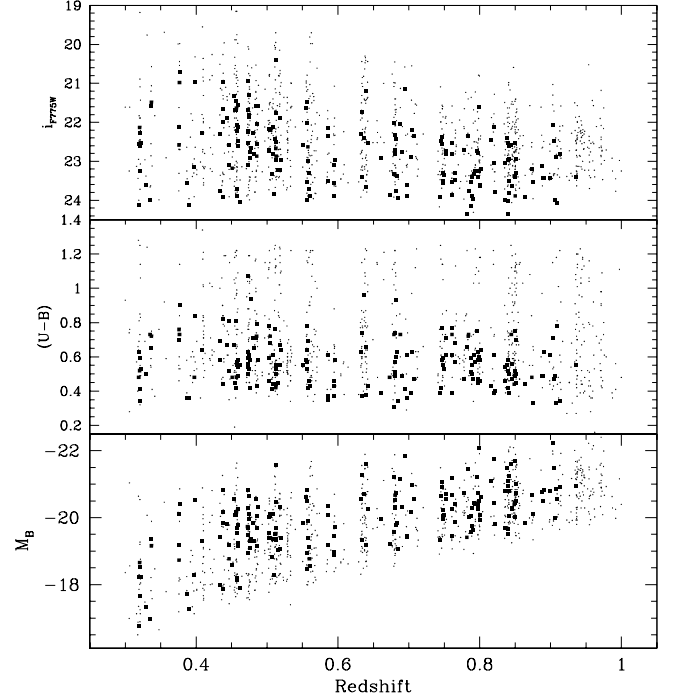


FIG. 2.—Distribution of apparent magnitude,  $U - B$  color, and  $B$ -band luminosity as a function of redshift for 204 galaxies selected for chemical analysis (*large symbols*) and the 1044 objects in the TKRS survey with spectroscopic redshifts  $0.3 < z < 1.0$  (*dots*).

bluest (i.e., most actively star-forming) galaxies from  $0.3 < z < 1.0$ .

## 2.2. Emission-Line Measurements and Uncertainties

We utilized the boxcar-extracted (not the optimally extracted) one-dimensional spectra made publicly available by the TKRS Team. We manually measured equivalent widths<sup>5</sup> of the  $[O II] \lambda\lambda 3726, 3729$ ,  $H\beta$ , and  $[O III] \lambda 5007$  emission lines present in each of the TKRS spectra with the IRAF *splot* routine using Gaussian fits with variable baseline, width, and height. The  $[O II] \lambda\lambda 3726, 3729$  doublet, when spectrally resolved, was fitted with a blend of two Gaussian profiles. Visual inspection of this doublet showed that the  $\lambda\lambda 3726/3729$  ratio, where sufficiently resolved, was always consistent with low electron densities of less than a few hundred  $\text{cm}^{-3}$ . We required that the fits to the  $H\beta$  and  $[O III] \lambda 5007$  lines have the same Gaussian width. This constraint helped to make EW measurements more robust when one or the other of these nebular lines was affected by night-sky emission lines. Table 1 lists the measured equivalent widths and measurement uncertainties for each line in columns (9)–(11). The reported equivalent widths are corrected from the observed to the rest frame using

$$EW_{\text{rest}} = \frac{EW_{\text{observed}}}{1 + z}. \quad (1)$$

In all cases, we add  $2 \text{ \AA}$  to the EW of  $H\beta$  as a general correction for underlying stellar absorption (see Ke03). The EW reported for  $[O III]$  in column (11) includes the (unmeasured)

<sup>5</sup> The TKRS spectra are not flux calibrated, so we use the equivalent widths of strong emission lines in our analysis, following the prescription of Kobulnicky & Phillips (2003).



contribution from [O III]  $\lambda 4959$  using the assumption that  $I([\text{O III}]_{\lambda 5007})/I([\text{O III}]_{\lambda 4959}) = 3$  so that

$$\begin{aligned} \text{EW}([\text{O III}]) &= 1.3 \times \text{EW}([\text{O III}]_{\lambda 5007}) \\ &= \text{EW}([\text{O III}]_{\lambda 5007}) + \text{EW}([\text{O III}]_{\lambda 4959}). \end{aligned} \quad (2)$$

In a few cases, the [O III]  $\lambda 5007$  line was hopelessly lost in the noise from imperfectly subtracted night-sky lines. For these objects,  $\text{EW}([\text{O III}])$  is measured using

$$\text{EW}([\text{O III}]) = 4 \times \text{EW}([\text{O III}]_{\lambda 4959}), \quad (3)$$

and such instances are denoted by the numeric code 2 in column (14) of Table 1. For 35 low-redshift objects, equivalent widths of the H $\alpha$  and [N II]  $\lambda 6584$  lines or upper limits could also be measured. The ratio  $\text{EW}_{\text{H}\alpha}/\text{EW}_{[\text{N II}]\lambda 6584}$  is recorded in column (12). Where only an upper limit on [N II]  $\lambda 6584$  could be measured, we give the  $3\sigma$  lower limits on the  $\text{EW}_{\text{H}\alpha}/\text{EW}_{[\text{N II}]\lambda 6584}$  ratio.

In 27 of the galaxies, only upper limits on [O III]  $\lambda 5007$  could be measured. These objects are located at the bottom of Table 1 and are denoted by the numeric code 3 in column (14). To avoid a potential metallicity bias in the sample, we include these objects in our analysis and list the  $3\sigma$  upper limits on the  $\text{EW}([\text{O III}])$  in column (11) of Table 1. The upper limits on [O III] (and [N II], where possible) are estimated by

$$\text{EW} = 3\text{RMS} \sqrt{1.8 \text{npix}_{\text{FWHM}}}, \quad (4)$$

where RMS is the rms in an offline region adjacent to the line and  $\text{npix}_{\text{FWHM}}$  is the number of pixels across the FWHM of the line profile, typically 4–10 pixels.

Associated uncertainties on each line EW in columns (9)–(11) are computed taking into account both the uncertainty on the line strength and the continuum level placement using

$$\sigma_{\text{EW}} = \sqrt{\frac{1}{C^2} \sigma_L^2 + \frac{L^2}{C^4} \sigma_C^2}, \quad (5)$$

where  $L$ ,  $C$ ,  $\sigma_L$ , and  $\sigma_C$  are the line and continuum levels in photons and their associated  $1\sigma$  uncertainties. We determine  $\sigma_C$  manually by fitting the baseline regions surrounding each emission line. We adopt  $\sigma_L = \text{RMS}(1.8 \text{npix}_{\text{FWHM}})^{1/2}$ . Using this empirical approach, the stated uncertainties implicitly include the *internal* error from one emission line relative to another due to Poisson noise, sky background, sky subtraction, read noise, and flat-fielding. In nearly all cases, the continuum can be fitted along a substantial baseline region, so that  $\sigma_C \ll \sigma_L$ . There are, however, additional uncertainties on the *absolute* values of the equivalent widths due to uncertainties on the continuum placement, particularly for the [O II]  $\lambda 3727$  line, which are difficult to include in the error budget.

Using the observed H $\beta$  equivalent widths and calculated blue luminosities, we estimate the SFR for each of the TKRS galaxies in our sample. The H $\beta$  luminosity is estimated as

$$L_{\text{H}\beta}(\text{ergs s}^{-1}) = 5.49 \times 10^{31} \times 2.5^{-M_B} \text{EW}_{\text{H}\beta}, \quad (6)$$

and then the SFR is calculated following Kennicutt (1998),

$$\text{SFR}(M_{\odot} \text{ yr}^{-1}) = \frac{2.8 L_{\text{H}\beta}}{1.26 \times 10^{41}}. \quad (7)$$

The resulting SFR estimates, in solar masses per year, appear in column (13) of Table 1. This is necessarily a lower limit on

the SFR because we do not correct for extinction or stellar absorption.

### 2.3. Additional Galaxies

To supplement the data on 204 TKRS galaxies analyzed here, we have collected the 64 emission-line measurements from the DGSS (Kobulnicky et al. 2003; Fig. 10, *filled symbols*), and additional objects from the CFRS from LCS03 and Carollo & Lilly (2001). We use the published emission-line measurements from those original works and include only the subset of those galaxies where the  $\text{EW}_{\text{H}\beta}$  is measured with an S/N of 8:1 or better, in keeping with our selection criteria described above.

### 2.4. Chemical Analysis

Following traditional nebular diagnostic techniques (e.g., Osterbrock 1989; Pagel et al. 1979) and extensions of these techniques for distant galaxies developed by Kobulnicky et al. (1999, hereafter KKP99) and Kobulnicky & Phillips (2003, hereafter KP03), we use the equivalent width ratios of the collisionally excited [O II]  $\lambda 3727$  and [O III]  $\lambda 4959$ ,  $5007$  lines relative to the H $\beta$  Balmer series recombination lines to estimate gas-phase oxygen abundances. The ratio of emission-line *equivalent widths*, while being one step further removed from the emission-line *flux ratios* calibrated against photoionization models, has the advantage of being reddening independent, to first order.

The principal diagnostic is the metallicity-sensitive emission-line ratio,

$$\log R_{23} \equiv \frac{I_{[\text{O II}]\lambda 3727} + I_{[\text{O III}]\lambda 4959} + I_{[\text{O III}]\lambda 5007}}{I_{\text{H}\beta}} \equiv x, \quad (8)$$

formulated by Pagel et al. (1979) and subsequently developed and recalibrated by many authors since (reviewed in KKP99). The  $R_{23}$  ratio is sensitive both to metallicity and to the ionization state of the gas, or “ionization parameter.” The ionization parameter ( $q$ ) is defined as

$$q = \frac{S_{\text{H}^0}}{n}, \quad (9)$$

where  $S_{\text{H}^0}$  is the ionizing photon flux passing through a unit area and  $n$  is the local number density of hydrogen atoms. This ionization parameter is divided by the speed of light to give the more commonly used ionization parameter;  $\mathcal{U} \equiv q/c$ . Some  $R_{23}$ –O/H calibrations have attempted to correct for the ionization parameter (e.g., McGaugh 1991; Kewley & Dopita 2002, hereafter KD02) by using the ratio of the oxygen lines, known as  $O_{32}$ :

$$\log O_{32} \equiv \log \left( \frac{I_{[\text{O III}]\lambda 4959} + I_{[\text{O III}]\lambda 5007}}{I_{[\text{O II}]\lambda 3727}} \right) \equiv y, \quad (10)$$

In Figure 3, we show the relationship between the  $R_{23}$  ratio and  $O_{32}$  for the TKRS galaxies. The colored curves represent the theoretical photoionization models calculated by (a) Kewley & Dopita (2002) and (b) McGaugh (1991). The grids in Figure 3a show the theoretical relationship between  $R_{23}$  and  $O_{32}$  for various values of metallicity mass fraction,  $Z$ , and ionization parameter,  $q$ . For reference, the metal mass fraction,  $Z$ , is related to the oxygen abundance,  $12 + \log(\text{O}/\text{H})$ , by

$$Z \simeq 29 \times 10^{[12 + \log(\text{O}/\text{H}) - 12]} \quad (11)$$

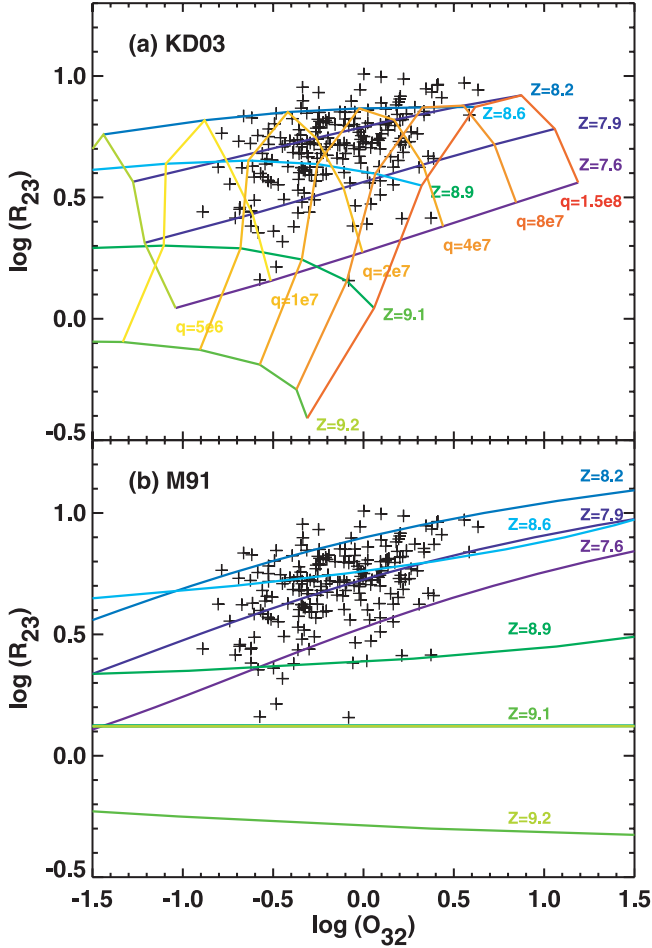


FIG. 3.—Logarithm of the metallicity-sensitive line ratio  $R_{23}$  vs. the logarithm of the ionization parameter-sensitive ratio  $O_{32}$  for the TKRS galaxies. The colored curves represent the theoretical photoionization models of (a) Kewley & Dopita (2002) and (b) M91. Models are shown for metallicities between  $12 + \log(\text{O}/\text{H}) = 7.6$  (violet) and  $12 + \log(\text{O}/\text{H}) = 9.1$  (green). For reference, solar metallicity is  $12 + \log(\text{O}/\text{H}) \sim 8.7$  (Allende Prieto et al. 2001). The Kewley & Dopita (2002) models for ionization parameters between  $q = 5 \times 10^6$  and  $1.5 \times 10^8 \text{ cm s}^{-1}$  are shown (yellow-red curves). The TKRS data span ionization parameters  $q = (1-8) \times 10^7 \text{ cm s}^{-1}$ .

for the standard solar abundance distribution (e.g., Anders & Grevesse 1989) with the newer solar oxygen abundance of Allende Prieto et al. (2001), which yields a solar metallicity of  $Z_{\odot} \simeq 0.015$  and  $12 + \log(\text{O}/\text{H})_{\odot} = 8.72$ . The grid points for Figure 3 are provided in Table 2. The models predict an upper limit to  $\log R_{23}$ . This upper limit occurs because at low metallicity the intensity of the forbidden lines scales roughly with the chemical abundance while at high abundance the nebular cooling is dominated by the infrared fine-structure lines and the electron temperature becomes too low to collisionally excite the optical forbidden lines. The position of the theoretical upper limit is similar for the Kewley & Dopita (2002) and McGaugh (1991) models. A few of the TKRS galaxies have a  $\log R_{23}$  maximum that is slightly higher by  $\sim 0.1-0.2$  dex than the theoretical limits. The theoretical models were calculated assuming that the star formation occurred in an instantaneous burst. This assumption may be reasonable for H II regions or for galaxy spectra dominated by one or two H II regions. However, continuous burst models may be more appropriate for modeling the emission-line spectra of active star-forming galaxies (e.g., Kewley et al. 2001). Continuous burst models would increase the theoretical upper limit by  $\sim 0.2$  dex, making the data consistent with model limits (L. J. Kewley 2004, in preparation). We will compute new metallicity diagnostics utilizing continuous burst models in a future paper.

Figure 3 illustrates the difficulty in using  $R_{23}$  to diagnose metallicity. Not only is  $R_{23}$  sensitive to the ionization parameter, but it is double valued in terms of the metallicity. To break the degeneracy, other metallicity-sensitive line ratios are required. For the 30 galaxies in our sample with measured  $[\text{N II}]/\text{H}\alpha$  ratios, we calculate an initial metallicity using the  $[\text{N II}]/\text{H}\alpha$  metallicity formulation from KD02. A further two galaxies have small  $[\text{N II}]/\text{H}\alpha$  upper limits that allowed us to break the  $R_{23}$  degeneracy. For the potential ionization parameter and metallicity range of our sample (Fig. 3), the KD02  $[\text{N II}]/\text{H}\alpha$ -metallicity relation can be parameterized as

$$\begin{aligned}
 12 + \log(\text{O}/\text{H}) = & 7.04 + 5.28X_{\text{N II}} + 6.28X_{\text{N II}}^2 + 2.37X_{\text{N II}}^3 \\
 & - \log q(-2.44 - 2.01X_{\text{N II}} \\
 & - 0.325X_{\text{N II}}^2 + 0.128X_{\text{N II}}^3) \\
 & + 10^{X_{\text{N II}} - 0.2} \log(q)(-3.16 + 4.65X_{\text{N II}}),
 \end{aligned} \tag{12}$$

TABLE 2  
 $O_{32}$  AND  $R_{32}$  VALUES FOR CURVES SHOWN IN FIGURE 3

$q$ ( $\text{cm s}^{-1}$ )	LINE RATIO	$Z$						
		0.05	0.1	0.2	0.5	1.0	1.5	2.0
$5 \times 10^6$ .....	$\log O_{32}$	-1.03	-1.21	-1.27	-1.43	-1.59	-1.72	-1.87
	$\log R_{23}$	0.04	6.67	8.76	2.60	2.26	5.54	5.57
$1 \times 10^7$ .....	$\log O_{32}$	-0.51	-0.61	-0.76	-0.87	-1.09	-1.10	-1.33
	$\log R_{23}$	0.16	5.79	8.99	6.62	2.76	5.47	4.0
$2 \times 10^7$ .....	$\log O_{32}$	-0.00	-0.11	-0.26	-0.41	-0.63	-0.68	-0.90
	$\log R_{23}$	0.27	6.18	7.91	3.72	4.50	5.63	6.28
$4 \times 10^7$ .....	$\log O_{32}$	0.44	0.33	0.17	-0.02	-0.25	-0.34	-0.57
	$\log R_{23}$	0.38	5.37	6.36	7.01	4.10	5.11	5.10
$8 \times 10^7$ .....	$\log O_{32}$	0.85	0.72	0.55	0.33	0.07	-0.09	-0.37
	$\log R_{23}$	0.48	9.72	4.80	4.25	6.01	5.19	4.59
$1.5 \times 10^8$ .....	$\log O_{32}$	1.19	1.06	0.87	0.62	0.32	0.06	-0.31
	$\log R_{23}$	0.56	6.22	6.73	8.04	6.68	5.30	9.91

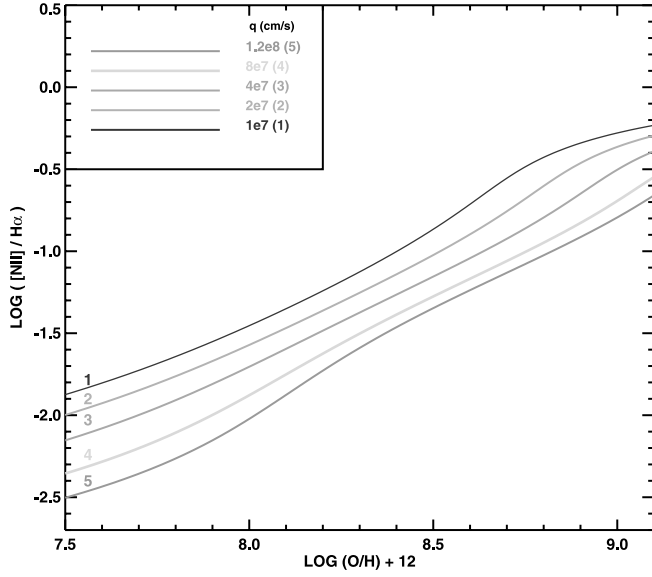


FIG. 4.—Metallicity-sensitive line ratio  $[\text{N II}]/\text{H}\alpha$  vs. metallicity  $12 + \log(\text{O}/\text{H})$ . The curves show our new parameterization (eq. [12]) to the theoretical photoionization models of Kewley & Dopita (2002) for various values of ionization parameter,  $q$ , in  $\text{cm s}^{-1}$  shown in the legend. Note that the  $[\text{N II}]/\text{H}\alpha$  ratio is very sensitive to the ionization parameter and is not a robust indicator of metallicity. The metallicity corresponding to any particular value of  $[\text{N II}]/\text{H}\alpha$  spans 0.4–0.6 dex in  $\text{O}/\text{H}$ , depending on ionization parameter. [See the electronic edition of the *Journal* for a color version of this figure.]

where  $X_{\text{N II}} = \log \text{EW}([\text{N II}]_{6584}/\text{EW}(\text{H}\alpha))$ . The ionization parameter is calculated from the KD02  $[\text{O III}]/[\text{O II}]-q$  relation, which we parameterize as

$$\begin{aligned} \log(q) = & \{32.81 - 1.153y^2 \\ & + [12 + \log(\text{O}/\text{H})](-3.396 - 0.025y + 0.1444y^2)\} \\ & \times \{4.603 - 0.3119y - 0.163y^2 \\ & + [12 + \log(\text{O}/\text{H})](-0.48 + 0.0271y + 0.02037y^2)\}^{-1}, \end{aligned} \quad (13)$$

where  $y = \log O_{32}$ . Figures 4 and 5 show the parameterizations in equations (12) and (13) for various values of ionization parameter. Equation (12) is only valid for ionization parameters  $q$  between  $5 \times 10^6$  and  $1.5 \times 10^8 \text{ cm s}^{-1}$ . KD02 show that for  $\log([\text{N II}]/\text{H}\alpha) > -0.8$ , the  $[\text{N II}]/\text{H}\alpha$  metallicity relationship breaks down. Although such high  $[\text{N II}]/\text{H}\alpha$  ratios indicate that the metallicity is on the upper branch [ $12 + \log(\text{O}/\text{H}) > 8.4$ ],  $[\text{N II}]/\text{H}\alpha$  cannot be used to estimate a metallicity in this regime. At lower  $[\text{N II}]/\text{H}\alpha$  values, the  $[\text{N II}]/\text{H}\alpha$  ratio is less sensitive to metallicity and is more dependent on the ionization parameter than the  $R_{23}$  ratio. Therefore,  $[\text{N II}]/\text{H}\alpha$  should only be used as a crude initial estimate for a more sensitive metallicity diagnostic such as  $R_{23}$ .

Because the  $[\text{N II}]/\text{H}\alpha$  ratio depends strongly on the ionization parameter and the  $[\text{O III}]/[\text{O II}]$  ratio depends on metallicity, we iterated equations (12) and (13) until the metallicity varied less than the model errors ( $\sim 0.1$  dex). Typically, 2–3 iterations were required. The resulting metallicity estimates indicate that 29 of 32 (91%) of the galaxies with usable  $[\text{N II}]/\text{H}\alpha$  ratios or upper limits lie on the upper  $R_{23}$  branch [ $12 + \log(\text{O}/\text{H}) > 8.4$ ]. In column (20) of Table 1 we list the oxygen abundance derived from the strength of the  $[\text{N II}] \lambda 6584/\text{H}\alpha$  equivalent width ratios for the 35 (necessarily the lowest

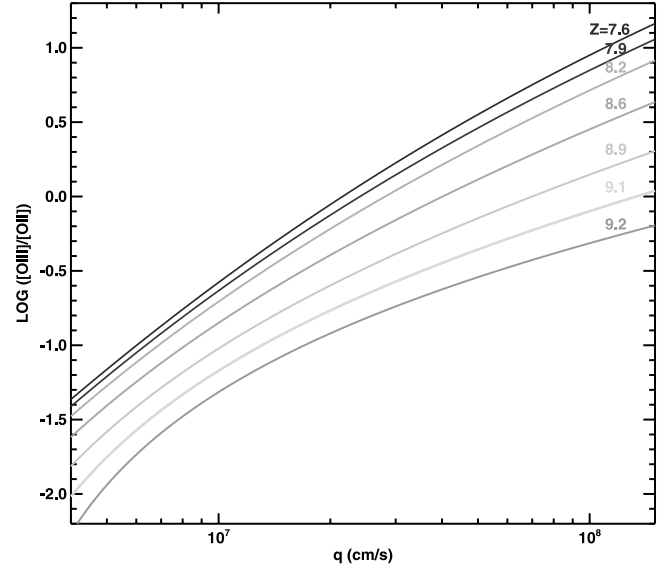


FIG. 5.— $[\text{O III}]/[\text{O II}]$  ratio vs. ionization parameter,  $q$ , in  $\text{cm s}^{-1}$ . The colored curves show our new parameterization (eq. [13]) to the theoretical photoionization models of Kewley & Dopita (2002) for various values of metal mass fraction,  $Z$ , shown. The relation between  $Z$  and  $\text{O}/\text{H}$  is discussed in § 2.4 and eq. (11). [See the electronic edition of the *Journal* for a color version of this figure.]

redshift) galaxies for which these lines can be measured. In many cases, only 3  $\sigma$  upper limits on the  $[\text{N II}] \lambda 6584$  equivalent widths are measured, so only upper limits on the oxygen abundances are given. Of the galaxies where  $[\text{N II}]$  can be measured, only two of the least luminous galaxies ( $M_B \sim -17$ ) have  $[\text{N II}] \lambda 6584/\text{H}\alpha$  ratios consistent with very low metallicities that would place them on the lower branch of the  $R_{23}$ – $\text{O}/\text{H}$  calibration. These objects are noted in Table 1.

For the TKRS galaxies without  $[\text{N II}]/\text{H}\alpha$  ratios, we are unable to break the  $R_{23}$  degeneracy. We make the motivated assumption (see Kobulnicky & Zaritsky 1999; Kobulnicky et al. 2003) that these galaxies fall on the upper branch [ $12 + \log(\text{O}/\text{H}) > 8.4$ ] of the double-valued  $R_{23}$ – $\text{O}/\text{H}$  relation, consistent with the majority of galaxies in our sample with  $[\text{N II}]/\text{H}\alpha$  ratios. We next compute the oxygen abundances of TKRS galaxies using several different, independent but related  $R_{23}$ – $\text{O}/\text{H}$  calibrations from the literature.

#### 2.4.1. Zaritsky et al. (1994)

ZKH94 provide a simple analytic relation between  $\text{O}/\text{H}$  and  $R_{23}$  only without regard to ionization parameter:

$$\begin{aligned} 12 + \log(\text{O}/\text{H})_{\text{ZKH94}} = & 9.265 - 0.33R_{23} - 0.202R_{23}^2 \\ & - 0.207R_{23}^3 - 0.333R_{23}^4. \end{aligned} \quad (14)$$

The ZKH94 formula is an average of three previous calibrations in the literature, namely, Dopita & Evans (1986), McCall et al. (1985), and Edmunds & Pagel (1984). Figure 6 shows these relations. The ZKH94 average relation was compared with a sample of disk  $\text{H II}$  regions with metallicities  $\log(\text{O}/\text{H}) + 12 > 8.35$ . As a result, the ZKH94 calibration is only suitable for  $\text{H II}$  regions in the metal-rich regime.

#### 2.4.2. McGaugh (1991)

McGaugh (1991, hereafter M91) calibrated the relationship between the  $R_{23}$  ratio and gas-phase oxygen abundance using

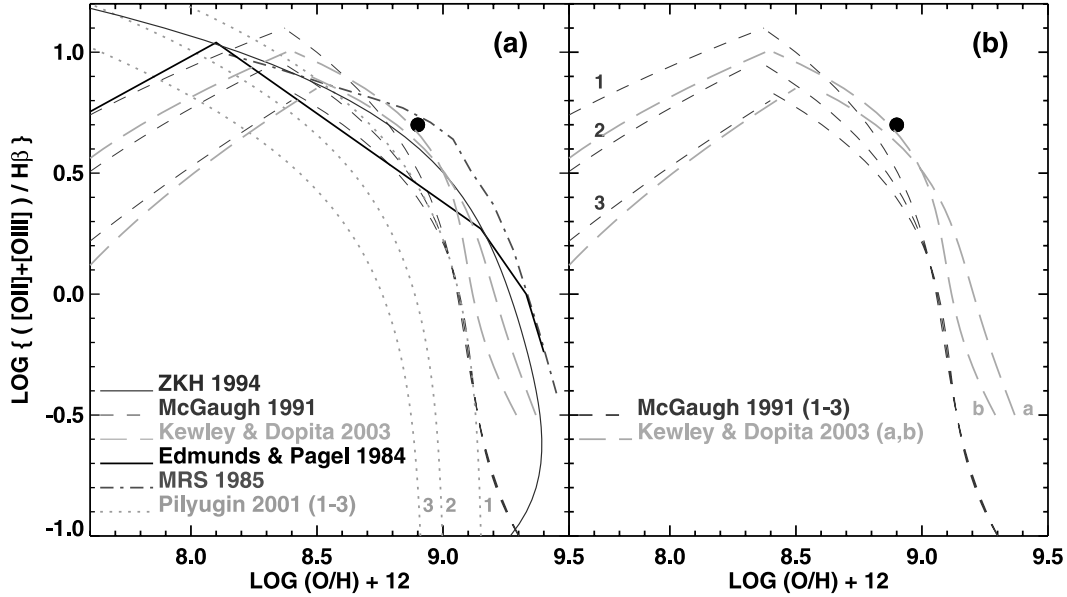


FIG. 6.—Metallicity calibration between strong-line ratio  $R_{23}$  and oxygen abundance,  $12 + \log(\text{O}/\text{H})$ , from several different authors as indicated in the legend. A solid circle marks the Orion Nebula value (based on data of Walter et al. 1992). For reference, the currently accepted value of solar abundance is  $12 + \log(\text{O}/\text{H})_{\odot} = 8.7$  (Allende Prieto et al. 2001). (a) Variation in  $R_{23}$  calibrations from the literature; (b) M91 and KD02 calibrations. The three curves labeled 1, 2, and 3 denote the Pilyugin (2001) and M91 models corresponding to  $\log O_{32} = 1, 0$ , and  $-1$ , respectively. Two curves labeled “a” and “b” denote the Kewley & Dopita (2002) models corresponding to ionization parameters of  $q = 1 \times 10^7$  and  $1.5 \times 10^8 \text{ cm s}^{-1}$ , respectively. [See the electronic edition of the *Journal* for a color version of this figure.]

H II region models from the photoionization code CLOUDY (Ferland & Truran 1981). McGaugh’s models include the effects of dust and variations in ionization parameter. We adopt the analytical expressions of S. McGaugh (1991, 1998 [private communication] as expressed in KKP99), which are based on fits to photoionization models for the metal-rich (upper) branch of the  $R_{23}$ –O/H relation. In terms of the reddening-corrected line intensities, this relation is

$$\begin{aligned}
 12 + \log(\text{O}/\text{H})_{\text{M91,upper}} = & 12 - 2.939 - 0.2x - 0.237x^2 \\
 & - 0.305x^3 - 0.0283x^4 \\
 & - y(0.0047 - 0.0221x - 0.102x^2 \\
 & - 0.0817x^3 - 0.00717x^4). \quad (15)
 \end{aligned}$$

Figure 6 shows graphically the relation between  $R_{23}$  and O/H for the M91 and other calibrations from the literature. A circle marks the Orion Nebula value (based on data of Walter et al. 1992), which is in excellent agreement with the most recent solar oxygen abundance measurement of  $12 + \log(\text{O}/\text{H})_{\odot} = 8.7$  (Allende Prieto et al. 2001). Oxygen abundances computed in this manner appear in Table 1 column (17), along with a  $1 \sigma$  uncertainty computed by propagating the uncertainties on the emission-line equivalent widths. This uncertainty estimate does not include the error introduced by the model uncertainties in the theoretical calibrations (typically  $\sim 0.1$  dex).

#### 2.4.3. Pilyugin (2001)

Pilyugin (2001) developed an  $R_{23}$ –O/H calibration based on a sample of H II regions with measurements of the [O III]  $\lambda 4363$  auroral line. The [O III]  $\lambda 4363$  auroral line provides a “direct” measurement of the electron temperature of the gas and, therefore, the metallicity. The use of the [O III]  $\lambda 4363$  auroral line to derive metallicities is known as the  $T_e$  method. Pilyugin

(2001) calculated direct metallicities for a sample of H II regions spanning  $8.2 \lesssim 12 + \log(\text{O}/\text{H}) \lesssim 8.6$ . His resulting  $R_{23}$ –O/H calibration provides three curves, depending on a parameter  $P$  that accounts for the range in ionization parameter in the H II regions. Pilyugin was unable to provide a fit to H II regions for  $12 + \log(\text{O}/\text{H}) \gtrsim 8.6$  because high-metallicity galaxies have weak or undetectable [O III]  $\lambda 4363$  (see Stasińska 2002 for a discussion). Therefore, Pilyugin extrapolated the  $8.2 \lesssim 12 + \log(\text{O}/\text{H}) \lesssim 8.6$  curves to higher metallicities. The Pilyugin curves are discussed further in Kennicutt et al. (2003).

#### 2.4.4. Kewley & Dopita (2002)

Kewley & Dopita (2002) provide a suite of abundance calibrations depending on the availability of particular nebular emission lines. Their calibrations are based on a combination of stellar population synthesis models (Pégase and STARBURST99) and detailed photoionization models using the MAPPINGS code (Sutherland & Dopita 1993). Like M91, the KD02 models include the effects of dust. KD02 include separate calibrations for the ionization parameter. KD02 point out that the  $R_{23}$  curve is dependent on the ionization parameter, while the common ionization parameter diagnostic ( $O_{32}$ ) depends on metallicity. They advocate the use of an iterative scheme to solve for both quantities if only [O III], [O II], and H $\beta$  are available. We provide a new parameterization of the KD02  $R_{23}$  method (from § 4.3 in KD02) with a form similar to that of the M91 calibration to facilitate metallicity estimation and comparisons with estimates made using M91. For the potential ionization parameter and metallicity range of our sample (Fig. 3), the lower branch [ $12 + \log(\text{O}/\text{H}) < 8.4$ ] is parameterized by

$$\begin{aligned}
 12 + \log(\text{O}/\text{H})_{\text{KD03,lower}} = & 9.40 + 4.65x - 3.17x^2 \\
 & - \log(q)(0.272 + 0.547x \\
 & - 0.513x^2), \quad (16)
 \end{aligned}$$

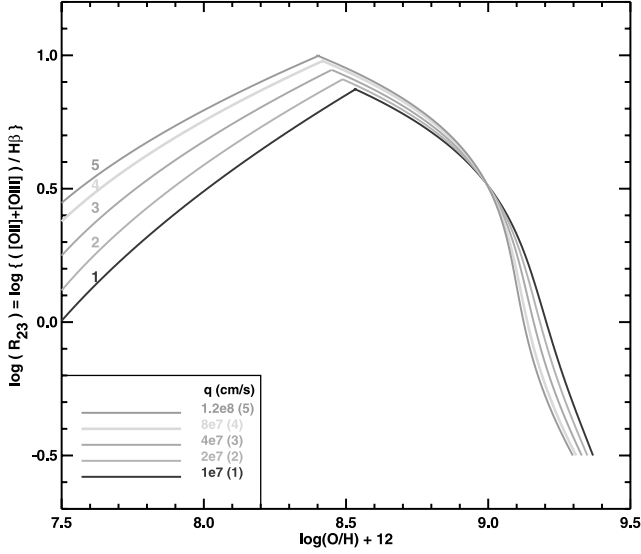


FIG. 7.—Metallicity-sensitive line ratio  $R_{23}$  vs. metallicity  $12 + \log(\text{O}/\text{H})$ . The colored curves show our new parameterization (eq. [17]) to the theoretical photoionization models of Kewley & Dopita (2002) for various values of ionization parameter,  $q$ , in  $\text{cm s}^{-1}$  shown in the legend. [See the electronic edition of the Journal for a color version of this figure.]

where  $x = \log R_{23}$ . The upper branch [ $12 + \log(\text{O}/\text{H}) \geq 8.4$ ] is parameterized by

$$12 + \log(\text{O}/\text{H})_{\text{KD03,upper}} = 9.72 - 0.777x - 0.951x^2 - 0.072x^3 - 0.811x^4 - \log q(0.0737 - 0.0713x - 0.141x^2 + 0.0373x^3 - 0.058x^4). \quad (17)$$

Figure 7 shows graphically the relation between the metallicity and  $R_{23}$  from equation (17) for various values of ionization parameter  $q$ . The ionization parameter,  $q$ , is found using equation (13) in an iterative manner. Typically, 2–3 iterations were required to reach convergence. This new parameterization is an improvement over the tabulated model coefficients of the KD02 calibration because (1) the new calibration does not fix the ionization parameter or metallicity to the finite set of model values during iteration and (2) there is an increased sensitivity to the metallicity around the local maximum ( $Z = 8.4$ ) because we have introduced different equations for the two branches rather than being limited to one equation. Oxygen abundances calculated via this method are given in column (18) of Table 1. This parameterization should be regarded as an improved, implementation-friendly approach to be preferred over the tabulated  $R_{23}$  coefficients of KD02.

#### 2.4.5. “Best” Adopted Oxygen Abundances

Of all the above methods for oxygen abundance computation, many arguments could be made for which are the “best” or most “accurate.” In Figure 8 we compare the “ $P$ -method,” M91, ZKH94, and KD02  $R_{23}$  metallicity estimates for the TKRS data. Differences between published calibrations shown in Figure 8 serve to illustrate the magnitude and severity of the possible systematic errors introduced by the different calibrations. The uncertainties from any published calibration method are dominated by systematic uncertainties and/or biases in the data and/or models used to construct the calibration. The  $P$ -method produces a strong systematic offset and large scatter

in the metallicity estimates compared to the three other calibrations. This offset probably occurs because the  $P$ -method was not calibrated using any data or theoretical models for the metallicity range of our sample. We therefore do not use the  $P$ -method in our preferred metallicity estimates.

The three remaining calibrations show smaller systematic offsets that are consistent with the error estimates of the calibrations ( $\sim 0.1$  dex). Principal differences among the models include different photoionizing radiation fields from the various stellar atmospheres, stellar libraries, and stellar tracks. Different photoionization models employ various atomic data and dust prescriptions. Different calibration data from observations of Galactic or extragalactic H II regions over a range of metallicities and ionization parameters may also affect the resulting calibrations. Analyzing the nuances and resolving the differences between the published strong-line–metallicity calibrations is beyond the scope of this work. The exact choice of metallicity calibration is not crucial to the first of the two goals in this paper. *Relative* differences in metallicity between samples at different redshifts will not be sensitive to the exact form of the  $R_{23}$ –O/H calibration adopted. Section 3 deals primarily with this question. Any of the three above methods that require only measurements of  $R_{23}$  and  $O_{32}$  will suffice for discerning trends with redshift.

Kennicutt et al. (2003) and Garnett et al. (2004) present evidence from observations of metal-rich H II regions in M51 and M101 that there is a discrepancy of several tenths of a dex (factor of 2 or more) between the metallicities derived using traditional strong-line methods and models and metallicities derived using direct measurements of [N II] electron temperatures. See these works for an extensive discussion regarding possible systematic effects in the  $R_{23}$ –O/H calibrations. *Hence, absolute metal abundances may have systematic uncertainties of 0.2–0.5 dex, particularly at the high-metallicity end of our sample.* Until these initial results are confirmed and a more robust calibration is available, we proceed to adopt a combination of the KD02 and M91 strong-line formulation.

For the purposes of providing the most meaningful metallicities to aid in modeling of distant galaxies, we adopt a final “best estimate” oxygen abundance by averaging the KD02 and M91  $R_{23}$  methods;  $12 + \log(\text{O}/\text{H})_{\text{avg}} = 1/2[12 + \log(\text{O}/\text{H})_{\text{KD03}} + \log(\text{O}/\text{H})_{\text{M91}}]$ . We use the new KD02 parameterization (eqs. [17] and [13]). Because the ZKH94 parameterization is based on an ad hoc average of three relatively old models and calibrations, we do not consider it for our best estimate in light of improvements to photoionization models (see, e.g., Dopita et al. 2000; Kewley et al. 2001 and references therein).

The resulting average abundances appear in Table 1. For  $12 + \log(\text{O}/\text{H}) > 8.4$ , the average of the KD02 and M91 methods can be approximated by the following simple form:

$$12 + \log(\text{O}/\text{H})_{\text{avg-upper}} \sim 9.11 - 0.218x - 0.0587x^2 - 0.330x^3 - 0.199x^4 - y(0.00235 - 0.01105x - 0.051x^2 - 0.04085x^3 - 0.003585x^4), \quad (18)$$

where  $x = \log R_{23}$  (eq. [8]) and  $y = \log O_{32}$  (eq. [10]). Note that this equation is only valid for the upper branch, and for the range of  $R_{23}$  and  $O_{32}$  values covered by our sample (Fig. 3).

#### 2.5. Comparison with Other Properties

Figure 9 shows the relations between the best estimate oxygen abundance, H $\beta$  equivalent width, SFR, absolute  $B$ -band

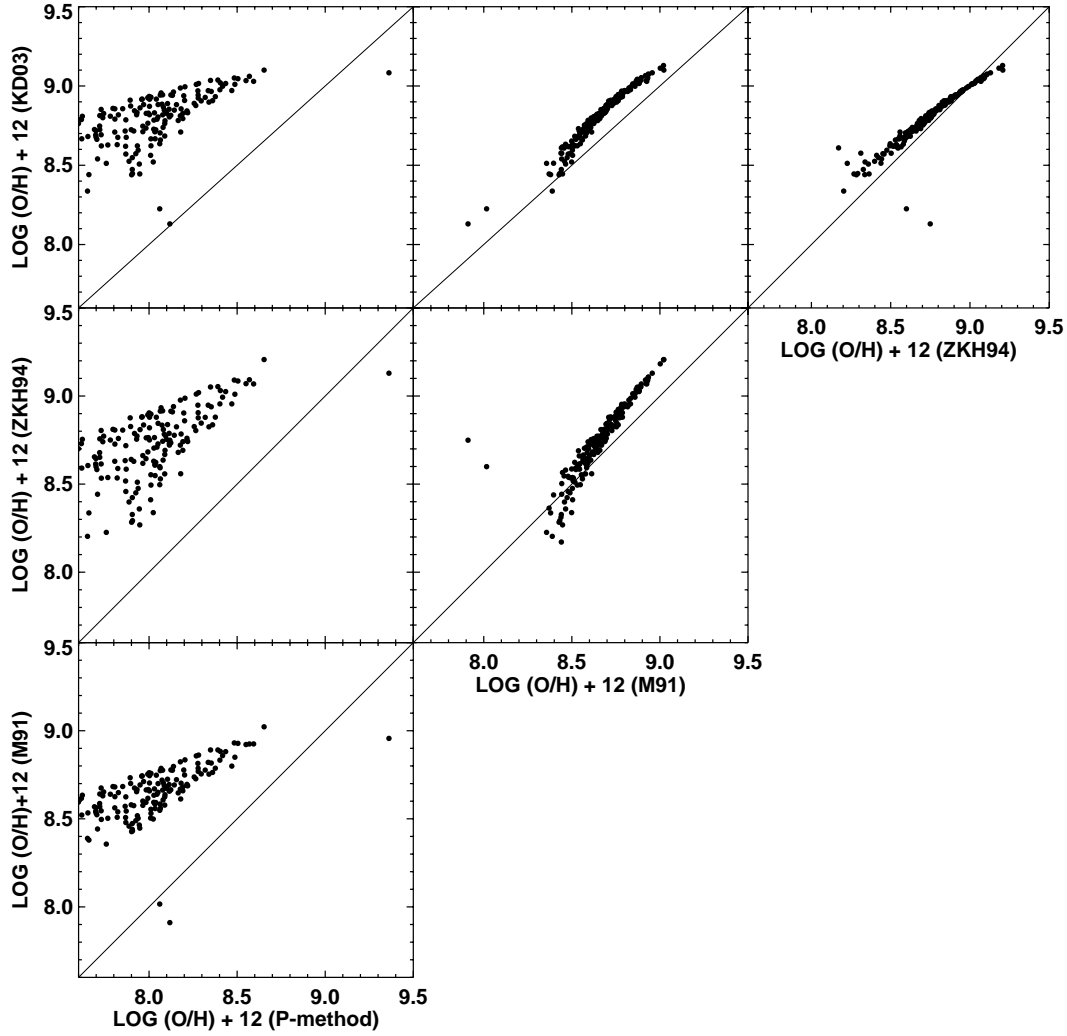


FIG. 8.—Comparison of difference oxygen abundance computation methods for TKRS galaxies. The solid  $y = x$  line indicates where the data would lie if the different metallicity estimates reach agreement. The  $P$ -method proposed by Pilyugin (2001) produces a strong systematic offset and significant scatter compared to the other three calibrations: M91, ZKH94, and KD02. Overall, the M91, ZKH94, and KD03 methods (with our new parameterization of the KD02  $R_{23}$  and  $[\text{O III}]/[\text{O II}]$  models) produce metallicity estimates that reach agreement to within the error estimates for the calibrations ( $\sim 0.1$  dex each). The ZKH94 method should not be used for  $12 + \log(\text{O}/\text{H}) < 8.35$  because the ZKH94 method places these galaxies on the upper  $R_{23}$  branch.

magnitude,  $U - B$  color, and redshift for the 204 selected TKRS galaxies. This figure illustrates that the colors and emission-line equivalent widths of selected TKRS galaxies are distributed approximately uniformly across the full observed range of parameter space within each redshift bin. It also shows that galaxies at increasingly higher redshifts tend to be more luminous and have higher SFRs.<sup>6</sup> This is a type of selection effect due to the magnitude-limited nature of the spectroscopic TKRS sample.

### 3. The $L$ - $Z$ Relation at $0.3 < z < 1.0$

#### 3.1. Evolution of the $L$ - $Z$ Relation

The addition of 204 new metallicities at  $0.3 < z < 1.0$  allows us to explore more robustly than before the chemoluminous evolution of galaxies over the last 8 Gyr. Figure 10 shows the oxygen abundance,  $12 + \log(\text{O}/\text{H})_{\text{M91}}$ , versus  $M_B$  for four redshift ranges. Filled symbols show the DGSS data

from Kobulnicky et al. (2003), crosses denote the CFRS data of LCS03 and CL01, and open symbols denote the TKRS data. Stars in the lower right panel are the  $z > 2$  Lyman break galaxies from Kobulnicky & Koo (2000) and Pettini et al. (2001). The dashed lines, which are the same in each panel, represent the fits to local emission-line galaxy samples as described in Kobulnicky et al. (2003). The solid lines are fits to the DGSS data alone. The new TKRS data are in good agreement with the previous  $L$ - $Z$  relations found for each redshift interval. It becomes possible for the first time with these data to see the  $L$ - $Z$  correlation at redshifts  $z > 0.8$  in the lower right panel. The most significant departure from the DGSS  $L$ - $Z$  correlation seen in the TKRS data occurs in the  $0.4 < z < 0.6$  bin (*lower left panel*). There are galaxies located to the faint/metal-rich side of the best-fit line in the TKRS sample that do not appear in the DGSS sample. This scatter is present to a lesser extent in the  $0.6 < z < 0.8$  range (*upper right panel*). Examination of these objects in Table 1 reveals these to be mostly objects with extreme values of the ionization parameter indicator,  $O_{32}$ . Most of these galaxies have  $\log O_{32} < -0.5$ , placing them in a regime in which the correlation between  $R_{23}$  and  $\text{EW}_{R_{23}}$  (KP03, Fig. 5) has a large dispersion and a systematic deviation from

<sup>6</sup> Note that the absolute blue magnitudes and SFRs are closely coupled parameters, since  $M_B$  is used, along with  $\text{EW}_{\text{H}\beta}$ , to estimate the SFR. They are not independent parameters.

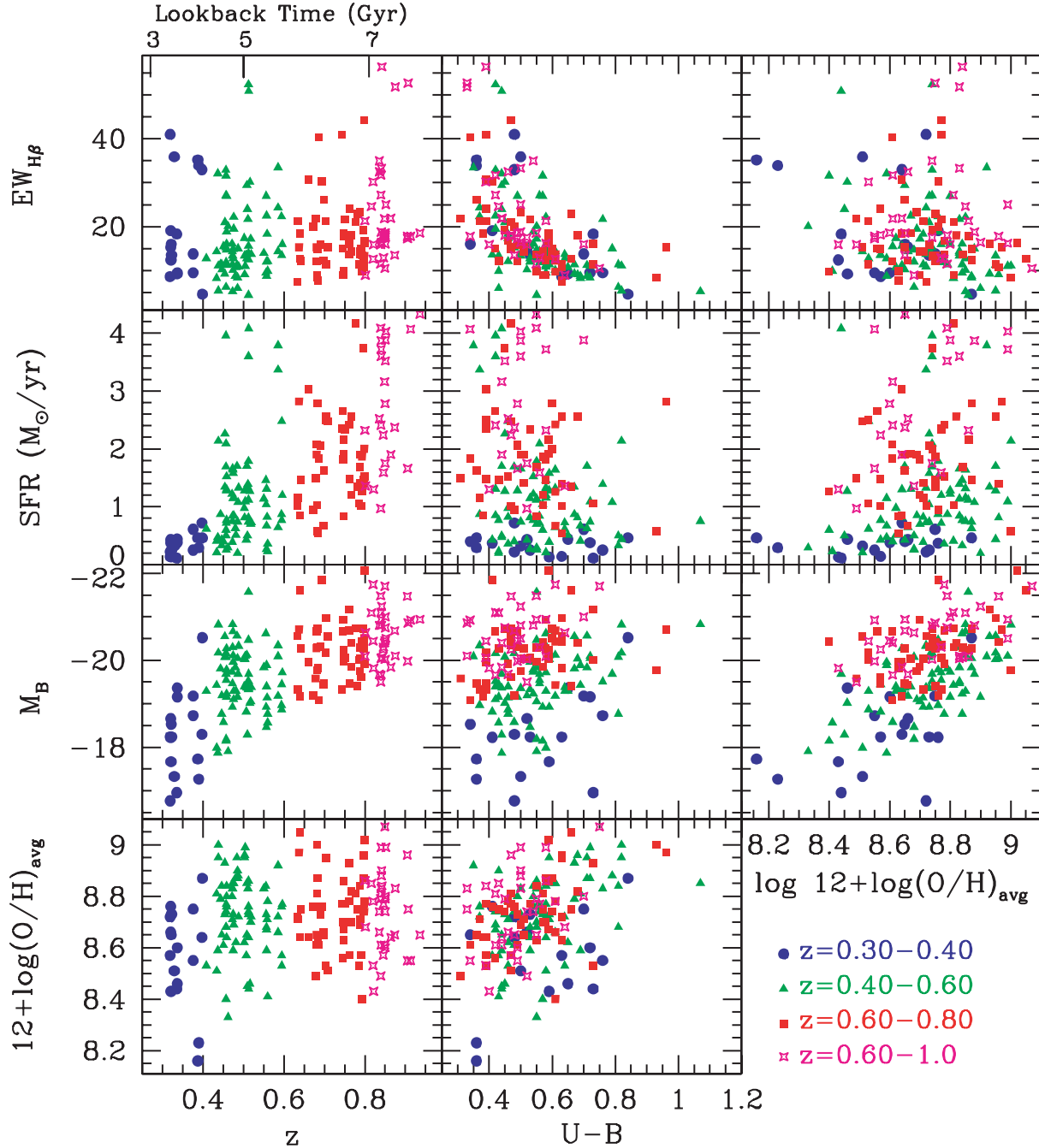


FIG. 9.—Distribution of  $H\beta$  equivalent width, SFR, absolute  $B$ -band magnitude, oxygen abundance,  $U-B$  color, and redshift for the 204 selected TKRS galaxies.

unity, making these points additionally uncertain. The conclusion of Figure 10 is to highlight the overall good correspondence of TKRS metallicities with other surveys for similar magnitude and redshift ranges.

Figure 11 shows our adopted oxygen abundances,  $12 + \log(O/H)_{\text{avg}}$ , for the DGSS+CFRS+TKRS galaxies versus  $M_B$  in each of four redshift intervals. Lines now represent fits to the combined data in each redshift interval. The dotted line is a fit of  $M_B$  on  $O/H$ ; the dashed line is the inverse fit of  $O/H$  on  $M_B$ . Since neither metallicity uncertainties nor the magnitude uncertainties are well characterized, we also use the method of linear bisectors described by Isobe et al. (1990; *solid line*). Parameters for the linear fits appear in Table 3. The fits show that, regardless of the fitting method adopted, there is evidence

that the slope of the  $L-Z$  correlation changes with redshift. For the linear bisector fits, the  $L-Z$  relation evolves monotonically from  $12 + \log(O/H) = (-0.164 \pm 0.031)M_B + 5.57$  in the lowest redshift bin to  $12 + \log(O/H) = (-0.241 \pm 0.030)M_B + 3.73$  in the highest redshift bin. For the  $O/H$  on  $M_B$  fits, the  $L-Z$  relation evolves monotonically from  $12 + \log(O/H) = (-0.074 \pm 0.032)M_B + 7.20$  in the lowest redshift bin to  $12 + \log(O/H) = (-0.134 \pm 0.032)M_B + 5.97$  in the highest redshift bin. This change is driven mainly by the appearance of a population of relatively luminous ( $M_B \sim -20$ ) but metal-poor [ $12 + \log(O/H) = 8.5-8.6$ ] galaxies in the two highest redshift bins. Ke03 reported this change in slope of the  $L-Z$  relation using data out to  $z = 0.8$ , and Figure 11 shows that this trend continues to higher redshifts. Based on plausible galaxy

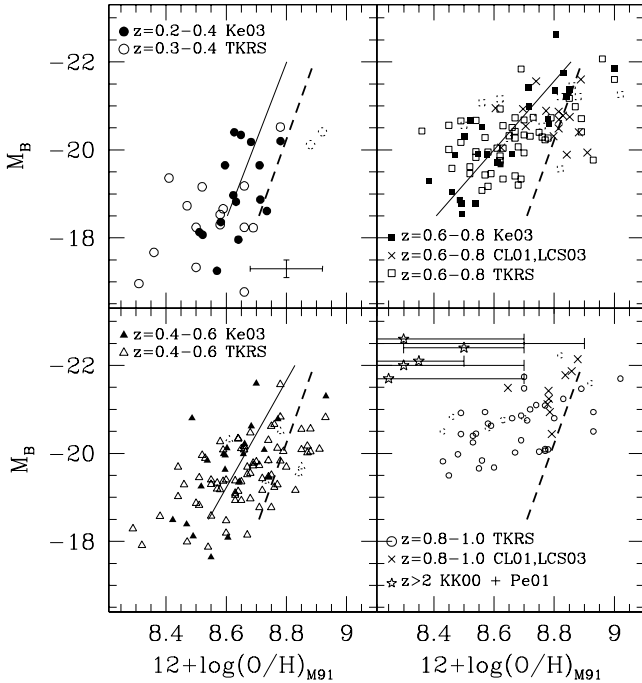


FIG. 10.—Relation between blue luminosity and oxygen abundance in four redshift bins for the TKRS galaxies in the GOODS-N field (*open symbols*), the DGSS from Kobulnicky et al. (2003; *filled symbols*), and the CFRS from Lilly et al. (2003; *crosses*) and Carollo & Lilly (2001; *crosses*). Dashed symbols denote  $3\sigma$  O/H lower limits for TKRS galaxies with  $[\text{O III}] \lambda 5007$  non-detections. Solid lines are fits to the DGSS data from Ke03, and dashed lines are fits to the local galaxies samples defined in Ke03. This figure shows oxygen abundances from col. (17) of Table 1. Stars denote the high-redshift  $z > 2$  galaxies from Kobulnicky & Koo (2000) and Pettini et al. (2001). The TKRS data are consistent with the previous results from smaller data sets.

evolution models, optical morphologies, and their present metallicities, this population of galaxies is likely to evolve at roughly constant luminosity into comparatively metal-rich disk galaxies in the local universe rather than fade into “dwarf” galaxies (see Ke03; LCS03).

The evolution of mean galaxy metallicity with redshift can be seen more easily in Figure 12, which shows oxygen abundance,  $12 + \log(\text{O}/\text{H})_{\text{avg}}$ , versus redshift for three different luminosity bins. The upper row displays only distant galaxies,  $z > 0.3$ . Lines show least-squares fits to the data with errors in O/H only. The left panel shows the lowest luminosity galaxies with  $-18.5 > M_B > -19.5$ . The slope of the least-squares linear fit is  $-0.19 \pm 0.10$  dex per unit redshift. The linear correlation coefficient for the 60 galaxies in this panel is  $-0.201$ , indicating that the probability of obtaining such a strong correlation at random is 12%. For the middle panel showing 100 galaxies in the luminosity range  $-19.5 > M_B > -20.5$ , the best-fit slope is  $-0.19 \pm 0.08$  dex per unit redshift. The correlation coefficient is  $-0.228$ , indicating that the probability of exceeding this degree of correlation by chance is 2%. For the right panel showing 69 galaxies in the luminosity range  $-20.5 > M_B > -21.5$ , the best-fit slope is  $-0.18 \pm 0.09$  dex per unit redshift. The correlation coefficient is  $-0.197$ , indicating that the probability of exceeding this degree of correlation by chance is 10%. Note that the relation between redshift and mean galaxy metallicity may not be (indeed, is theoretically not expected to be) a linear one if the SFR is not a linear function of redshift (e.g., Somerville et al. 2001). However, the observed dispersion and limited range of luminosity and redshift of the current data do not warrant additional parameters in the fit.

The lower row of Figure 12 shows the same galaxies as the upper row, but with the addition of local  $z = 0$  galaxies from Kennicutt (1992) and Jansen et al. (2000) used by Ke03 to define the local  $L$ - $Z$  relation. Lines show least-squares fits to the sample. The slopes are now somewhat smaller,  $0.14 \pm 0.05$  dex per unit redshift for the low- and intermediate-luminosity bins and  $0.13 \pm 0.05$  dex per unit redshift in the high-luminosity bin. This high-luminosity bin lacks the population of low-redshift ( $0.3 < z < 0.6$ ), low-metallicity [ $12 + \log(\text{O}/\text{H}) < 8.7$ ] galaxies present in the middle and left panels. It is this population, or rather the lack thereof, which is responsible for the change in slope of the  $L$ - $Z$  relation in Figures 10 and 11. The metallicities of the most luminous objects could be described as reaching a plateau near  $12 + \log(\text{O}/\text{H}) = 8.9$  with increasing scatter to lower oxygen abundances at larger redshifts. Such a plateau is expected in chemical evolution models as galaxies expend their gas supplies near the cessation of star formation activity. However, this plateau may also be a consequence of the  $R_{23}$  to O/H formulation (Fig. 6), which asymptotes at high metallicities, folded with observational selection effects, which will preferentially exclude very high metallicity objects that have very weak  $[\text{O III}]$  emission lines.

The mean rate of metal enrichment observed in Figure 12 is at least 0.14 dex per unit redshift for all luminosity bins. This rate of metal enrichment is significantly greater ( $2-3\sigma$ ) than the increase of  $0.08 \pm 0.02$  dex estimated by Lilly et al. (2003) over the same redshift interval. The smaller  $[d(\text{O}/\text{H})]/dz$  measured by LCS03 stems from the fact that (1) the mean luminosity of the LCS03 sample would lie in our high-redshift bin ( $-20.5 < M_B < -21.5$ ) and (2) LCS03 compare the oxygen abundance average (weighted by the  $\text{H}\beta$  luminosity) of relatively luminous  $M_B < -19.5$  CFRS galaxies with an average of NFGS galaxies spanning a range of luminosities from  $M_B = -16$  to  $-22$ . The inclusion of these low-luminosity galaxies in

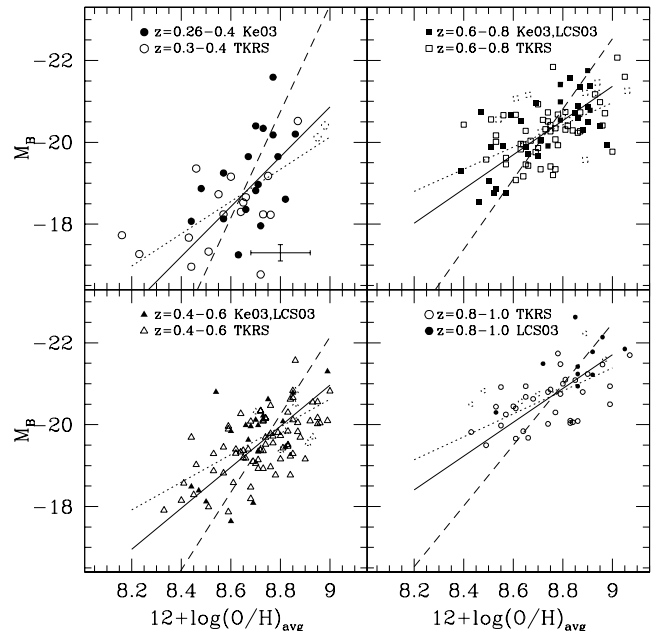


FIG. 11.—Relation between blue luminosity and oxygen abundance as in Fig. 10 except that oxygen abundances are  $(\text{O}/\text{H})_{\text{avg}}$  from col. (19) of Table 1. Dotted and dashed lines are linear least-squares fits for  $x$  on  $y$  and  $y$  on  $x$ , while the solid lines are linear bisectors of the two fits. Parameters of the fits appear in Table 3.



TABLE 3  
 $L$ - $Z$  RELATION FITS:  $12 + \log(\text{O}/\text{H})_{\text{avg}} = X \times M_B + Y$

Sample (1)	$z$ (2)	No. of Galaxies (3)	$X_{\text{avg}}$ (4)	$Y_{\text{avg}}$ (5)
O/H on $M_B$ Fits				
DGSS+CFRS+TKRS.....	0.2–0.4	32	$-0.077 \pm 0.032$	7.20
DGSS+CFRS+TKRS.....	0.4–0.6	97	$-0.105 \pm 0.017$	6.66
DGSS+CFRS+TKRS.....	0.6–0.8	84	$-0.117 \pm 0.017$	6.37
DGSS+CFRS+TKRS.....	0.8–1.0	44	$-0.134 \pm 0.032$	5.97
Linear Bisector Fits				
DGSS+CFRS+TKRS.....	0.2–0.4	32	$-0.164 \pm 0.026$	5.57
DGSS+CFRS+TKRS.....	0.4–0.6	97	$-0.199 \pm 0.016$	4.82
DGSS+CFRS+TKRS.....	0.6–0.8	84	$-0.239 \pm 0.029$	3.88
DGSS+CFRS+TKRS.....	0.8–1.0	44	$-0.241 \pm 0.027$	3.73

NOTE.—Col. (1): galaxy sample, by redshift; col. (2): redshift range; col. (3): number of galaxies in sample; col. (4): slope of metallicity-luminosity relation and uncertainty; col. (5): intercept of the least-squares fit.

the local mean reduces the metallicity difference between the local and distant samples.

### 3.2. The Effects of Sample Selection

Could some selection effect in the chosen galaxy sample produce the signature of evolution in the  $L$ - $Z$  relation? Kobulnicky et al. (2003) discuss possible selection effects in the DGSS sample and conclude that no identifiable selection effect can produce the observed signature of chemoluminous evolution with cosmic epoch. Here we test the TKRS sample for selection effects that could mimic the signature of genuine evolution in the  $L$ - $Z$  relation. Figure 13 shows the correlation between luminosity and  $12 + \log(\text{O}/\text{H})$  for 177 TKRS galaxies coded

by redshift interval. Dashed lines are unweighted linear least-squares fits of  $x$  on  $y$  and  $y$  on  $x$ , while the solid line is the linear bisector of the two fits. This figure shows that the highest redshift TKRS galaxies lie systematically to the bright/metal-rich side of the overall  $L$ - $Z$  relation. To examine whether some parameter other than redshift might be responsible for this trend, we show in Figure 14 the magnitude residuals from the best-fit  $L$ - $Z$  relation (Fig. 13, *solid line*) as a function of other fundamental galaxy parameters:  $M_B$ , SFR,  $U - B$  color, redshift, and ionization parameter indicator  $O_{32}$ . There is no correlation between magnitude residuals and  $U - B$  or  $O_{32}$ . There is a strong correlation between magnitude residuals and  $z$ , SFR, and  $M_B$ . These three parameters are not independent quantities. As

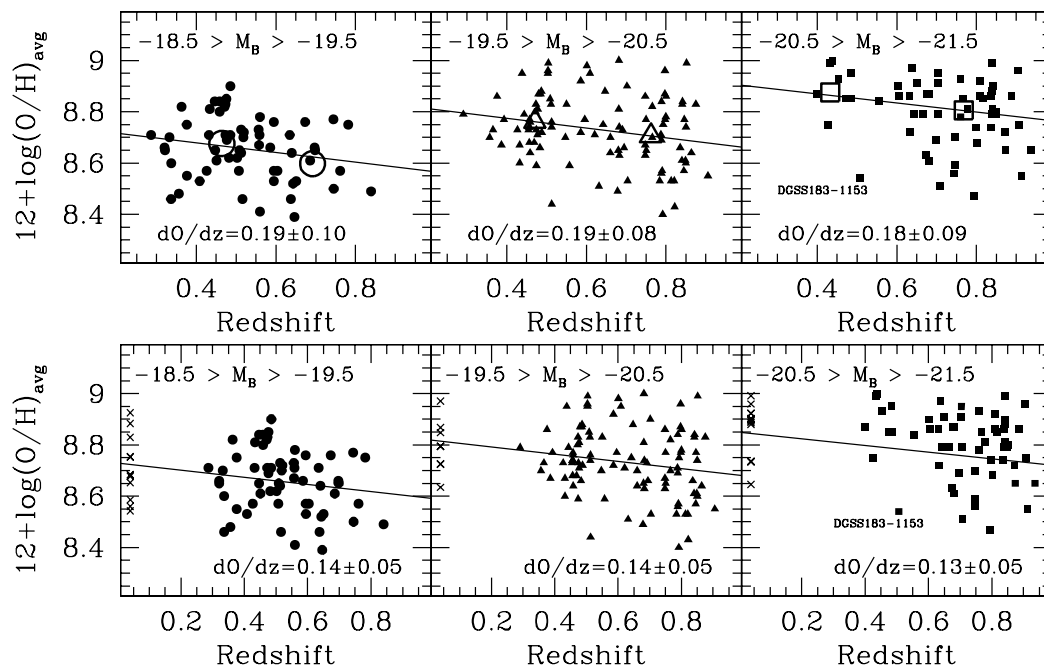


FIG. 12.—Relation between redshift and oxygen abundance for TKRS plus CFRS (LCS03) and DGSS (Ke03) galaxies in three different luminosity ranges. The upper row shows only distant galaxies. Large open symbols indicate mean values in two redshift bins:  $z < 0.6$  and  $z > 0.6$ . The lower row shows the same data with a sample of local  $z = 0$  galaxies from Jansen et al. (2000) and Kennicutt (1992) as defined by Ke03. The slopes of least-squares fits are given in each panel. The evolution of mean oxygen abundance with redshift is  $\sim 0.19$  dex per unit redshift in the upper row and is consistent across redshift bins. When local galaxies are considered, the slopes of the metallicity-redshift relations in all bins drop to  $\sim 0.14 \pm 0.05$  dex per unit redshift.

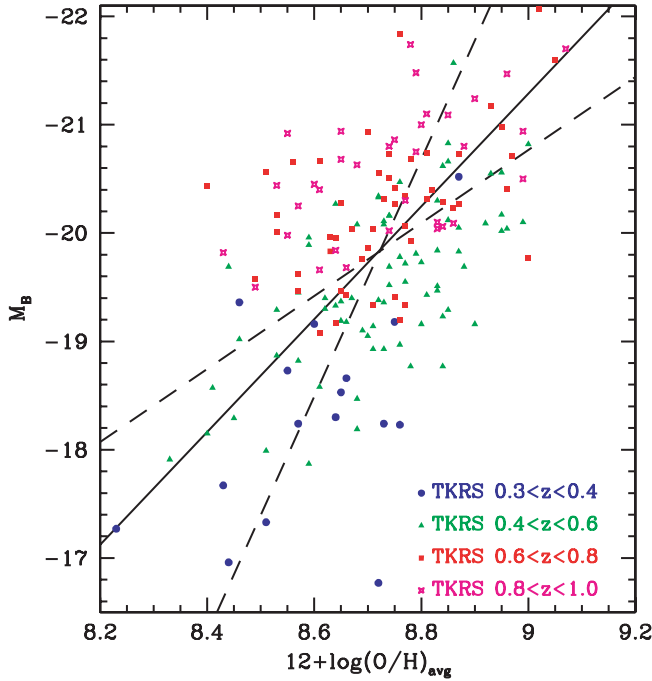


FIG. 13.— $L$ - $Z$  relation for 177 TKRS galaxies with symbols denoting the four redshift bins. Dashed lines are unweighted linear least-squares fits of  $x$  on  $y$  and  $y$  on  $x$ , while the solid line is the linear bisector of the two fits. This figure shows that the highest redshift TKRS galaxies lie systematically to the bright/metal-rich side of the overall  $L$ - $Z$  relation.

noted in the discussion of Figure 9,  $M_B$  is tightly coupled with SFR because it is used, along with  $EW_{H\beta}$ , to calculate the SFR. The SFR scales with  $M_B$ . Redshift and the mean  $M_B$  at a given redshift are also closely coupled by the characteristics of a magnitude-limited survey. Figures 2 and 9 illustrate that galaxies as faint as  $M_B = -17$  populate the lowest redshift bin while the highest redshift bin contains no objects fainter than  $M_B = -19.5$ . The lowest redshift bin also lacks the population of luminous  $M_B = -22$  galaxies found at larger distances. The correlations in Figure 14, then, may all be understood as a consequence of a single underlying cause, namely, the interrelation between  $z$ ,  $M_B$ , and SFR among sample galaxies.

Which of the three parameters is the fundamental one driving the observed change in the  $L$ - $Z$  relation? We argue that redshift is fundamental. Because the least-squares fit in Figure 13 uses  $M_B$  as one of the correlative variables, residuals should not depend on  $M_B$ . If the SFR were the fundamental parameter driving the evolution of the  $L$ - $Z$  relation (i.e., galaxies with the highest SFRs preferentially lie on the bright/metal-poor side of the  $L$ - $Z$  relation), then we would also expect related parameters such as the  $U - B$  color, which is sensitive to the SFR, to show a correlation with  $\Delta M_B$  as well. Figure 14 shows that  $U - B$  is not correlated with  $\Delta M_B$ . We are left with the conclusion that the evolution of the  $L$ - $Z$  relation is driven primarily by the redshift of the galaxies under consideration. Galaxies of a given luminosity are, on average, increasingly metal-poor at higher redshifts. Said another way, galaxies of a given metallicity are, on average, more luminous at higher redshifts. This effect is most pronounced among the least luminous galaxies, those with  $M_B$  fainter than  $\sim -20$ . None of the identified sample selection effects would produce the changes in the nature of the  $L$ - $Z$  relation seen in Figures 11 and 12.

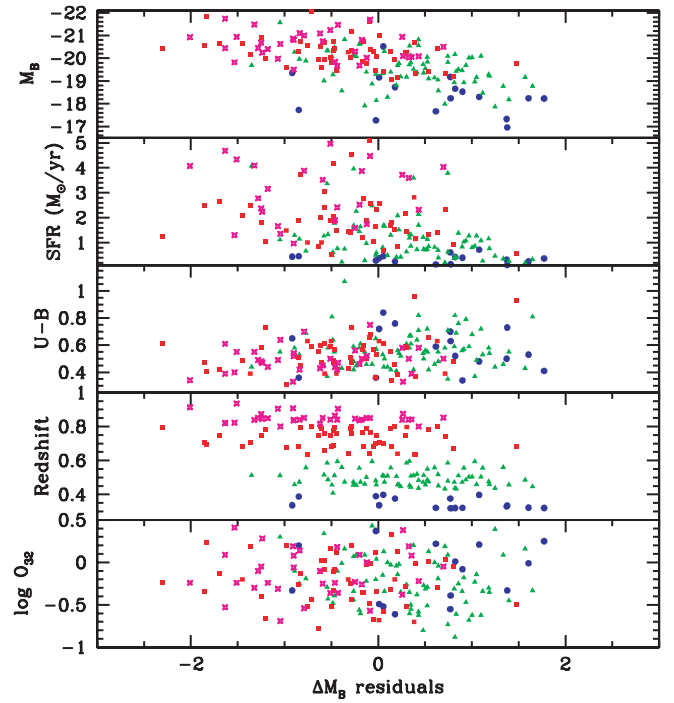


FIG. 14.—Magnitude residuals,  $\Delta M_B$ , from the best-fit luminosity-metallicity relation in Fig. 13 for 177 TKRS galaxies as a function of luminosity, SFR, color, redshift, and ionization parameter indicator,  $O_{32}$ . Symbols denote redshift bins. There is a strong correlation between magnitude residuals and the three closely related parameters  $z$ , SFR, and  $M_B$ . There is no correlation between residuals and  $U - B$  or  $O_{32}$ .

### 3.3. Comparison with Metallicity Evolution in the Milky Way

One goal of studying galaxy populations at cosmological distances is to understand the evolutionary paths of individual galaxies. However, observing the evolution of the mean chemoluminous properties of the population of star-forming galaxies over the last 8 Gyr (Figs. 11 and 12) is not the same thing as observing the evolution of any particular galaxy. Events shaping the evolution of any given galaxy at any particular point in its history could, in principle, be unique to that galaxy and not be reflected in the mean properties of galaxies at the equivalent look-back time in the distant universe. A galaxy may, for example, spend most of its existence in a quiescent passively evolving phase after a brief initial period of star formation. Other galaxies might form stars continuously throughout their existence, while still others may not begin the star formation process until comparatively recent times. However, if the boundary conditions for galaxy evolution are determined primarily by global cosmological parameters, such as the age of the universe, the expansion rate, and the density of dark matter and gas available to form stars, then the evolutionary paths of most galaxies ought to be observable in the mean evolution of galaxy properties with redshift.

Measuring ages and chemical abundances of stars in the Milky Way provides a glimpse into the history of one presumably typical disk galaxy. Figure 15 shows  $[O/H]$ , the logarithmic oxygen abundances relative to solar, of F and G stars in the Galactic disk as a function of age (Reddy et al. 2003). We have plotted on the ordinate the redshift corresponding to the look-back time of the measured age of the star. For our adopted cosmology of  $H_0 = 70 \text{ km s}^{-1} \text{ Mpc}^{-1}$ ,  $\Omega_M = 0.3$ , and  $\Omega_\Lambda = 0.7$ , the relation between redshift,  $z$ , and

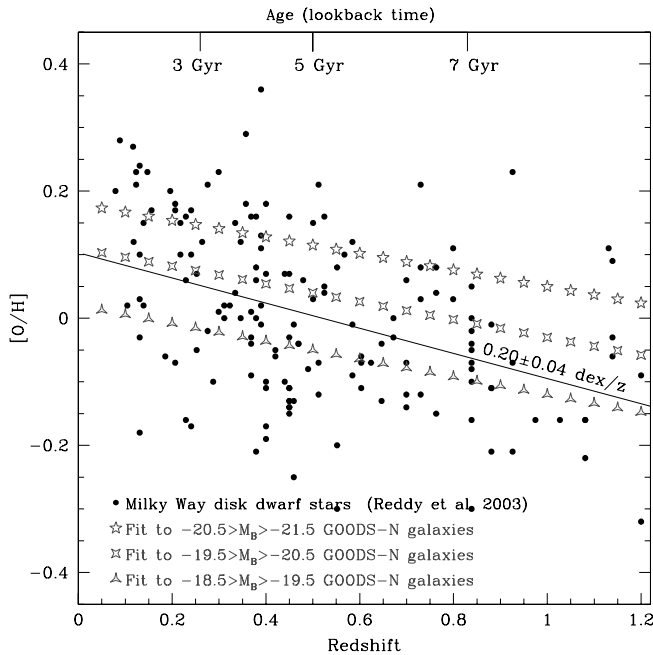


FIG. 15.—Relation between age (aka look-back time) and oxygen abundance, relative to solar, for Milky Way disk stars from Reddy et al. (2003). The ages of the stars are plotted in terms of their equivalent redshifts (using the adopted cosmology) for direct comparison with Fig. 12. The line shows a least-squares linear fit to the Galactic data. The tracks of symbols show the fits from Fig. 12 (lower row) for galaxies in three different luminosity bins. The mean slope and zero point for the evolution of Milky Way stars are in good agreement with the overall metallicity and rate of enrichment for distant galaxies. [See the electronic edition of the *Journal* for a color version of this figure.]

the look-back time or age,  $a$ , in Gyr is closely approximated by a polynomial,

$$z = 1.3356 - 2.0847a + 1.2431a^2 - 0.33620a^3 + 0.046737a^4 - 0.0032106a^5 + 0.000086938a^6. \quad (19)$$

The solid line shows the least-squares O/H on  $z$  fit to the stellar measurements. The tracks of starred symbols show the least-squares linear fits to distant GOODS-N+CFRS+TKRS galaxies in the three luminosity bins from the lower row of Figure 12. We use  $[O/H] = 12 + \log(O/H) - 8.7$  in keeping with the most recent solar oxygen abundance measurements (Allende Prieto et al. 2001). Both the overall level of metal enrichment (zero point) for  $M_B \sim 20$  galaxies and the rate at which oxygen abundance increases with time (slope) among all GOODS-N galaxies over the redshift range  $z = 1-0$  agree well with the trend observed in Galactic stars. The slopes of the best-fit relations for galaxies from the lower panel of Figure 12,  $0.14 \pm 0.05$  dex, are within the uncertainties of the slope for Milky Way stars,  $0.20 \pm 0.04$  dex over the range  $0.0 < z < 1.0$ .

LCS03 presented a diagram similar to Figure 15 in which they compare CFRS and NFGS oxygen abundances with  $[Fe/H]$  measurements of Galactic disk stars and noted that the stars were consistently 0.2–0.3 dex more metal-poor than the galaxies. This offset may be understood as the signature of supersolar O/Fe ratios found in Galactic stars over most of the history of the Milky Way reflecting varying nucleosynthetic sources (reviewed by Wheeler et al. 1989). Using oxygen measurements for Milky Way stars in Figure 15 shows good agreement with the oxygen abundance measurements in distant galaxies. While the luminosity history of the Milky Way is not

known and the dispersion in oxygen abundances for Galactic stars is large, the chemical enrichment process that occurred in the disk of the Milky Way appears to be a good representation of the chemical enrichment process in the bulk of the star-forming galaxies over the last 8 Gyr. Ke03 observed that the majority of the star-forming galaxies in the DGSS over a similar redshift range appeared to have substantial disk components on the basis of *Hubble Space Telescope* imaging. Thus, it appears that we are able to observe directly, in ensembles of disklike galaxies at cosmological distances, the same chemical histories encoded in Galactic stellar populations. In general, we expect that the luminosity-weighted nebular oxygen abundance of the entire Milky Way would be 0.1–0.3 dex higher than the metallicity of the solar neighborhood, given that the bulk of star formation occurs in the molecular ring at smaller radii where the average composition is more metal-rich (e.g., Shaver et al. 1983; Maciel et al. 2003).

For a galaxy that evolves as a “closed box” (i.e., no gas inflow or outflow), converting gas to stars with a fixed initial mass function (IMF) and chemical yield, the metallicity is determined by a single parameter: the gas mass fraction,  $\mu = M_{\text{gas}}/(M_{\text{gas}} + M_{\text{stars}})$ . The metallicity,  $Z$ , is the ratio of mass in elements heavier than He to the total mass and is given by

$$Z = Y \ln \frac{1}{\mu}, \quad (20)$$

where  $Y$  is the “yield” as a mass fraction. A typical total metal yield for a Salpeter IMF integrated over 0.2–100  $M_{\odot}$  is  $Y = 0.012$  by mass (i.e.,  $\frac{2}{3}$  the solar metallicity of 0.018; see Pagel 1997, Chap. 8). A total oxygen yield for the same IMF would be  $Y_O = 0.006$ . Effective yields in many local galaxies range from solar to factors of several lower (Kennicutt & Skillman 2001; Garnett 2002). The change in metallicity with gas mass fraction is independent of yield and is given by

$$\frac{d \log Z}{d \mu} = \frac{d}{d \mu} \left( Y \ln \frac{1}{\mu} \right) = \frac{0.434}{\mu \ln \mu}. \quad (21)$$

For reasonable values of the gas mass fraction (0.1–0.3), the change in gas mass fraction,  $\Delta \mu$ , corresponding to  $\Delta \log Z = 0.14$  is 0.07 to 0.12. Such a change in average gas content should be observable with future radio wave interferometers.

### 3.4. Comparison with Expectations of Cosmic Star Formation Models

The observed 0.14 dex increase in oxygen abundance of galaxies from  $z = 1$  to 0 is equivalent to a 38% increase in metallicity since  $z = 1$ . In other words, 28% of the metals in  $z = 0$  star-forming galaxies  $-18.5 < M_B < 20.5$  have been produced in the last 7.7 Gyr since  $z = 1$ . This conclusion can be tested for consistency against expectations from the global rate of cosmic star formation over the same period. Given that the magnitude range of our sample encompasses the bulk of luminosity produced by all galaxies (given a typical local galaxy luminosity function), the observed 28% increase in metal content should reflect the overall level of chemical enrichment in the universe. The rate of metal enrichment should correlate directly with the rate of star formation, subject to the condition that the stellar IMF and the chemical yield per mass of stars formed is constant.

The cosmic rate of star formation as a function of redshift has been extensively studied, and we adopt, for illustrative

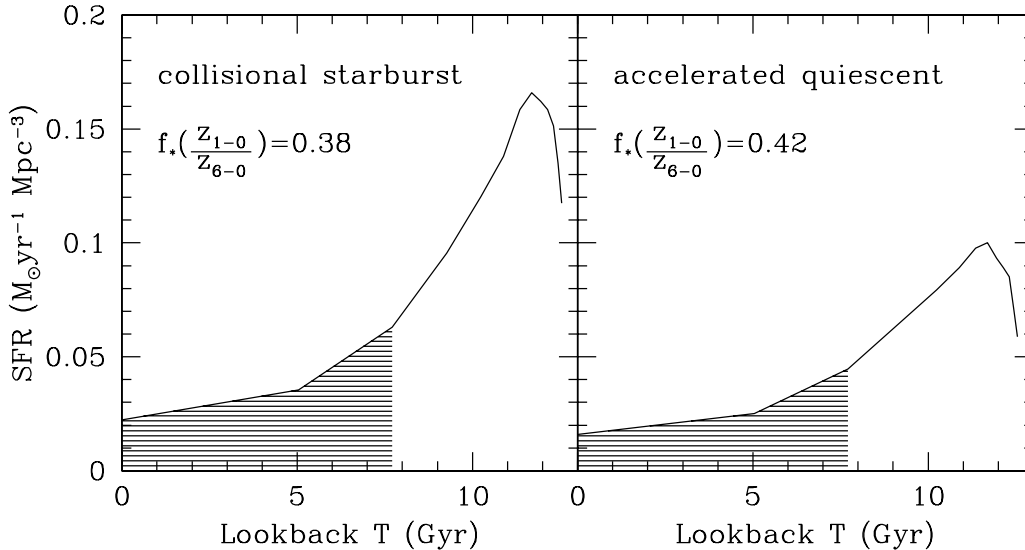


FIG. 16.—SFR density as a function of time, for our adopted cosmology, based on two models from Fig. 9 of Somerville et al. (2001). The shaded regions in each panel show the integral of the SFR over the period from  $z = 0$  to  $1$  (0–7.7 Gyr look-back time). The fraction of all stars formed in the last 7.7 Gyr,  $f_*[(z_{1-0})/(z_{6-0})]$ , is 0.38 and 0.42, respectively, for the “collisional starburst” and “accelerated quiescent” models.

purposes, the models from Figure 9 of Somerville et al. (2001). Figure 16 shows the SFR versus time for their “collisional starburst” and “accelerated quiescent” models, which give reasonable agreement with the observations. We have transformed redshift into linear time on the ordinate, using our adopted cosmology, and plotted linear SFR on the abscissa. The shaded regions in each figure show the integral of the SFR over time from  $z = 0$  to  $1$  (0–7.7 Gyr look-back time). The fraction of all stars formed in the last 7.7 Gyr,  $f_*[(z_{1-0})/(z_{6-0})]$ , is 0.38 and 0.42 in the two models. This fraction compares favorably with the fraction of metals formed during the same time period,  $0.28 \pm 0.07$ , from the previous section. Any difference, if real, between the predicted fraction based on SFR indicators and the observed fraction may be explained in several ways.

1. The present data/models may be underestimating the fraction of star formation that occurred before  $z = 1$ . An SFR that is, on average, not more than 10% higher at  $z > 1$  would be required to produce agreement.

2. The stellar IMF or metal yield may vary with redshift so that the assumption of a linear relationship between star and metal production is violated. A stellar IMF that is more shallow or more top heavy, or a higher effective nucleosynthetic yield at  $z > 1$  would be required.

Given the significant uncertainties on the SFR and the metal enrichment rate in galaxies as a function of redshift, no firm conclusion can be drawn except to say that the two rates are generally consistent with one another. Given that all models and data on the SFR (e.g., see Fig. 16 and the summary in Somerville et al. 2001) show a decline in the SFR with time after  $z = 1$ , the rate of metal enrichment in galaxies should also drop. In principle, this drop in the rate of metal enrichment should be observable in chemical studies of galaxies at cosmological distances but will require a level of measurement precision and/or a sample size beyond current capabilities.

#### 4. DISCUSSION

Our findings with the GOODS-N data here are in agreement with the conclusions of Ke03, namely, that chemoluminous evolution is most pronounced among the least luminous (and

possibly the least massive) galaxies during the 8 Gyr since  $z \sim 1$ . The change in slope of the  $L$ - $Z$  relation with redshift in Figure 11 is due to the emergence of a population of moderately luminous ( $M_B \sim -20$ ) galaxies with intermediate metallicities [ $12 + \log(\text{O}/\text{H}) \sim 8.5\text{--}8.6$ ] at redshifts beyond  $z = 0.6$ , which are not seen in local samples. This observation is consistent with the conclusions of LCS03, who advocate a progression of star formation activity from massive galaxies to less massive galaxies with decreasing redshift, a process generically termed as “downsizing” (Cowie et al. 1996). In the context of single-zone Pégase2 galaxy evolution models, Kobulnicky et al. (2003) concluded that the change in slope of the  $L$ - $Z$  relation could be explained by at least two of the following three phenomena: (1) low-mass galaxies have lower effective chemical yields than massive galaxies, (2) low-mass galaxies assemble on longer timescales than massive galaxies, and (3) low-mass galaxies began the assembly process at a later epoch than massive galaxies, i.e., “downsizing.” The possibility that low-mass galaxies begin their assembly at a later cosmic epoch has received several independent sources of support, both theoretical and observational. Babul & Rees (1992) proposed a theoretical model whereby photoionization from the first generations of cosmic star formation keeps gas in galaxies with small potential wells ionized (and thus unable to form stars) until some relatively late epoch, approximately  $z = 1$ . Skillman et al. (2003) concluded from a *Hubble Space Telescope* study of the star formation history in the Local Group galaxy IC 1613 that its star formation may have been inhibited until  $z \sim 1$ . Kodama et al. (2004) concluded from color-magnitude relations that galaxies in the Subaru/XMM Deep Survey were consistent with a downsizing scenario as well.

Can the evidence for the downsizing scenario be predicted or modeled theoretically? Theoretical hydrodynamic simulations have been used recently to predict the variation of metallicity with redshift for damped Ly $\alpha$  (DLA) absorbers (e.g., Nagamine et al. 2004) or for the stellar metallicity of galaxies (e.g., Nagamine et al. 2001). Unfortunately, the current models suffer from a lack of resolution in the  $0 < z < 1$  range. The direct simulations by Nagamine et al. predict that the mean metallicity at  $z = 1$  is  $\sim 0.4 Z_\odot$ , corresponding to  $\log(\text{O}/\text{H}) + 12 \sim 8.3$ ,

significantly lower than the metallicities of our sample, even at  $z$  close to 1. However, both absorption-line measurements and simulations of chemical abundances in DLA systems are not directly comparable to emission-line measurements because the former probe the more extended gaseous halos surrounding galaxies while the latter probe the H II regions and sites of active star formation within the inner disks of galaxies. These chemical measurements of galaxies in the GOODS-N provide a significant data set for comparison with future cosmological simulations that will have the temporal and spatial resolution to track the composition of the galaxies on 10 kpc scales with redshift.

## 5. CONCLUSIONS

We have parameterized an updated analytic formulation of the  $R_{23}$ –O/H relations for estimating nebular oxygen abundances based on the photoionization models of Kewley & Dopita (2002). After reviewing existing calibrations, we also provide a parameterization for the average of this calibration and that of McGaugh (1991) for the upper branch only. An additional parameterization may be used to estimate, albeit very crudely, the metallicities of galaxies on the basis of nebular [N II]/H $\alpha$  ratios.

Analyzing spectra of 204 galaxies at  $0.3 < z < 1.0$  from the GOODS-N TKRS, we measure galaxy-averaged nebular oxygen abundances of  $8.2 < 12 + \log(\text{O}/\text{H}) < 9.1$ , corresponding to metallicities between 0.3 and 2.5 times the solar value. The overall oxygen abundance of galaxies in the luminosity range  $-18.5 < M_B < -21.5$  increases by  $0.14 \pm 0.05$  dex from  $z = 1$  to 0. Said another way, galaxies in this intermediate-redshift sample are 1–3 mag more luminous at a given metallicity than are local counterparts. For closed-box

chemical evolution models, the implied change in gas mass fraction,  $\mu$ , over the  $z = 1$ –0 interval as gas is cycled through stars to produce heavy elements is  $\Delta\mu \sim 0.10$ . This sample of galaxies exhibits a luminosity-metallicity correlation but with different zero points and possibly different slopes at each redshift interval. The change in slope is driven mostly by the appearance of a population of moderate-luminosity ( $M_B \sim -20$ ) galaxies at  $z > 0.6$  with intermediate metallicities [ $12 + \log(\text{O}/\text{H}) = 8.5$ –8.6]. This population is likely to evolve into the comparatively luminous, metal-rich disk galaxy population of today. This change in galaxy populations is consistent with a later formation epoch for lower mass galaxies. The increase in the mean oxygen abundance of  $-18.5 < M_B < -21.5$  galaxies is broadly consistent with the global picture of cosmic star formation activity, which suggests that  $\sim 38\%$  of the stars and  $\sim 28\% \pm 0.07\%$  of the metals in the universe have formed in the 7.7 Gyr since  $z = 1$ .

We thank David Koo for scientific inspiration and Christopher Willmer for the use of his  $K$ -correction code. We are grateful to the TKRS Team, the W. M. Keck Observatory Director, and the DEEP2 Redshift Survey Team for making these data possible and for making them available in a timely fashion to the larger astronomical community. We thank Danny Dale, Christy Tremonti, Alice Shapley, and Henry Lee for helpful conversations. Simon Lilly, the referee, provided key insights that improved the clarity and completeness of this paper. H. A. K. was supported by NASA through NRA-00-01-LTSA-052. L. J. K. was supported by a Harvard-Smithsonian CfA Fellowship.

## REFERENCES

- Allende Prieto, C. A., Lambert, D. L., & Asplund, M. 2001, *ApJ*, 556, L63  
 Anders, E., & Grevesse, N. 1989, *Geochim. Cosmochim. Acta*, 53, 197  
 Babul, A., & Rees, M. J. 1992, *MNRAS*, 255, 346  
 Bruzual, G., & Charlot, S. 2003, *MNRAS*, 344, 1000  
 Carollo, C. M., & Lilly, S. J. 2001, *ApJ*, 548, L153 (CL01)  
 Cowie, L. L., Songalia, A. A., Hu, E. M., & Cohen, J. G. 1996, *AJ*, 112, 839  
 Davis, M., et al. 2003, *Proc. SPIE*, 4834, 161  
 Dopita, M. A., & Evans, I. N. 1986, *ApJ*, 307, 431  
 Dopita, M. A., Kewley, L. J., Heisler, C. A., & Sutherland, R. S. 2000, *ApJ*, 542, 224  
 Dwek, E. 1998, *ApJ*, 501, 643  
 Edmunds, M. G., & Pagel, B. E. J. 1984, *MNRAS*, 211, 507  
 Faber, S. M. 1973, *ApJ*, 179, 423  
 Faber, S. M., et al. 2003, *Proc. SPIE*, 4841, 1657  
 Ferland, G. J., & Truran, J. W. 1981, *ApJ*, 244, 1022  
 Fioc, M., & Rocca-Volmerange, B. 1999, preprint (astro-ph/9912179)  
 Garnett, D. R. 2002, *ApJ*, 581, 1019  
 Garnett, D. R., Kennicutt, R. C., Jr., & Bresolin, F. 2004, *ApJ*, 607, L21  
 Giavalisco, M., et al. 2004, *ApJ*, 600, L93  
 Hippelein, H., et al. 2003, *A&A*, 402, 65  
 Isobe, T., Feigelson, E. D., Akritas, M. G., & Babu, G. J. 1990, *ApJ*, 364, 104  
 Issa, M. R., MacLaren, I., & Wolfendale, A. W. 1990, *A&A*, 236, 237  
 Jansen, R. A., Franx, M., Fabricant, D., & Caldwell, N. 2000, *ApJS*, 126, 271 (NFGS)  
 Kennicutt, R. C., Jr. 1992, *ApJS*, 79, 255  
 ———. 1998, *ApJ*, 498, 541  
 Kennicutt, R. C., Jr., Bresolin, F., & Garnett, D. R. 2003, *ApJ*, 591, 801  
 Kennicutt, R. C., Jr., & Skillman, E. D. 2001, *AJ*, 121, 1461  
 Kewley, L. J., & Dopita, M. A. 2002, *ApJS*, 142, 35 (KD02)  
 Kewley, L. J., Dopita, M. A., Sutherland, R. S., Heisler, C. A., & Trevena, J. 2001, *ApJ*, 556, 121  
 Kobulnicky, H. A., Kennicutt, R. C., Jr., & Pizagno, J. 1999, *ApJ*, 514, 544 (KKP99)  
 Kobulnicky, H. A., & Koo, D. C. 2000, *ApJ*, 545, 712 (KK00)  
 Kobulnicky, H. A., & Phillips, A. C. 2003, *ApJ*, 599, 1031 (KP03)  
 Kobulnicky, H. A., & Zaritsky, D. 1999, *ApJ*, 511, 118 (KZ99)  
 Kobulnicky, H. A., et al. 2003, *ApJ*, 599, 1006 (Ke03)  
 Kodama, T., et al. 2004, *MNRAS*, 350, 1005  
 Lequeux, J., Peimbert, M., Rayo, J. F., Serrano, A., & Torres-Peimbert, S. 1979, *A&A*, 80, 155  
 Lilly, S. J., Le Fèvre, O., Crampton, D., Hammer, F., & Tresse, L. 1995, *ApJ*, 455, 50  
 Lilly, S. M., Carollo, C. M., & Stockton, A. N. 2003, *ApJ*, 597, 730 (LCS03)  
 Leitherer, C., et al. 1999, *ApJS*, 123, 3 (Starburst99)  
 Maciel, W. J., Costa, R. D. D., & Uchida, M. M. 2003, *A&A*, 397, 667  
 Maier, C., Meisenheimer, K., & Hippelein, H. 2004, *A&A*, 418, 475  
 Matthews, W. G., & Baker, J. C. 1971, *ApJ*, 170, 241  
 McCall, M. L., Rybski, P. M., & Shields, G. A. 1985, *ApJS*, 57, 1 (MRS)  
 McGaugh, S. 1991, *ApJ*, 380, 140 (M91)  
 Mehlert, D., et al. 2002, *A&A*, 393, 809  
 Nagamine, K., Fukugita, M., Cen, R., & Ostriker, J. P. 2001, *ApJ*, 558, 497  
 Nagamine, K., Springel, V., & Hernquist, L. 2004, *MNRAS*, 348, 435  
 Nishi, N., & Tashiro, M. 2000, *ApJ*, 537, 50  
 Osterbrock, D. E. 1989, *Astrophysics of Gaseous Nebulae and Active Galactic Nuclei* (Mill Valley: University Science Books)  
 Pagel, B. E. J. 1997, *Nucleosynthesis and Chemical Evolution of Galaxies* (Cambridge: Cambridge Univ. Press), 217  
 Pagel, B. E. J., Edmunds, M. G., Blackwell, D. E., Chun, M. S., & Smith, G. 1979, *MNRAS*, 189, 95  
 Pettini, M., Shapley, A. E., Steidel, C. C., Cuby, J.-G., Dickinson, M., Moorwood, A. F. M., Adelberger, K. L., & Giavalisco, M. 2001, *ApJ*, 554, 981 (Pe01)  
 Pilyugin, L. S. 2001, *A&A*, 374, 412  
 Prévot, M. L., Lequeux, J., Maurice, E., Prévot, L., & Rocca-Volmerange, B. 1984, *A&A*, 132, 389  
 Reddy, B. E., Tomkin, J., Lambert, D. L., & Allende Prieto, C. 2003, *MNRAS*, 340, 304  
 Rowan-Robinson, M. 2001, *ApJ*, 549, 745  
 Savaglio, S., et al. 2004, *ApJ*, 602, 51  
 Shapley, A. E., Erb, D. K., Pettini, M., Steidel, C. C., & Adelberger, K. L. 2004, *ApJ*, 612, 108  
 Shaver, P. A., McGee, R. X., Newton, L. M., Danks, A. C., & Pottasch, S. R. 1983, *MNRAS*, 204, 53

- Silva, L., Granato, G. L., Bressan, A., & Danese, L. 1998, *ApJ*, 509, 103
- Skillman, E. D., Kennicutt, R. C., Jr., & Hodge, P. 1989, *ApJ*, 347, 875
- Skillman, E. D., Tostoy, E., Cole, A. A., Dolphin, A. E., Saha, A., Gallagher, J. S., Dohm-Palmer, R. C., & Mateo, M. 2003, *ApJ*, 596, 253
- Somerville, R. S., Primack, J. R., & Faber, S. M. 2001, *MNRAS*, 320, 504
- Stasińska, G. 2002, in *Rev. Mex. AA Ser. Conf. 12, Ionized Gaseous Nebulae*, ed. W. J. Henney et al. (Mexico, DF: UNAM), 62
- Steidel, C., Shapley, A. E., Pettini, M., Adelberger, K. L., Erb, D. K., Reddy, M. A., & Hunt, M. P. 2004, *ApJ*, 604, 534
- Sullivan, M., Treyer, M. A., Ellis, R. S., & Mobasher, B. 2004, *MNRAS*, 350, 21
- Sutherland, R. S., & Dopita, M. A. 1993, *ApJS*, 88, 253
- Tinsley, B. M. 1974, *ApJ*, 192, 629
- . 1980, *Fundam. Cosmic Phys.*, 5, 287
- Vader, P. 1987, *ApJ*, 317, 128
- van Dokkum, P., et al. 2004, *ApJ*, 611, 703
- Walter, D. K., Dufour, R. J., & Hester, J. J. 1992, *ApJ*, 397, 196
- Wheeler, J. C., Sneden, C., & Truran, J. W. 1989, *ARA&A*, 27, 279
- Wirth, G. D., et al. 2004, *AJ*, submitted
- Woosley, S. E., & Weaver, T. A. 1995, *ApJS*, 101, 181
- Zaritsky, D., Kennicutt, R. C., Jr., & Huchra, J. P. 1994, *ApJ*, 420, 87 (ZKH94)